A New Light Weight Structural Material for Nuclear Structures

Nuclear Energy Enabling Technologies

Afsaneh Rabiei

North Carolina State University

In collaboration with:

None

Sue Lesica, Federal POC
Jeremy Busby, Technical POC

NEUP | Nuclear Energy University Programs

U.S. Department of Energy

FINAL REPORT

A New Light Weight Structural Material for Nuclear Structures

Prepared by:

Dr. Afsaneh Rabiei [PI] (arabiei@ncsu.edu)

Shuo Chen, PhD (graduate student supported by this grant)

Mechanical and Aerospace Engineering

North Carolina State University

911 Oval Drive, Raleigh, NC 27695-7910

Performed Under:

NEUP #CFP-11-1643

TPOC: Jeremy Busby

January 14, 2016

A New Light Weight Structural Material for Nuclear Structures

TABLE OF CONTENTS

LIST OF FIGURES

LIST OF TABLES

CHAPTER 1   EXECUTIVE SUMMARY

Report Organization

This report is organized as follows:

Ch. 2: Introduction

Ch. 3: Materials Processing and Characterization

Ch. 4**:** Experiments

Ch. 5**:** Results and Discussions

Ch. 6: Modeling and Simulation

Ch. 7: Summary and Conclusions

Milestones

1. Experimental works includes manufacturing close-cell composite metal foams (CMFs) with various sphere sizes of 2.2, 4, 5.2mm outer diameter by casting and powder metallurgy, as well as open-cell Al foam infiltrated with variety of different fillings: wax, polyethylene, water and borated water.

2. Radiation shielding will be evaluated by using standard gamma ray sources, a high-resolution microcomputed tomography (microCT) system as well as neutron attenuation using the NCSU 1-MW PULSTAR reactor.

3. Computational modeling using XCOM code for X ray and gamma ray transmission and Monte Carlo N-Particle transport code for neutron transmission to simulate the properties of the new material.

4. Experimental and modeling evaluation of thermal properties of composite foams including, thermal conductivity, thermal diffusivity, flame test and the effect of various parameters on such properties. The parameters that may vary are including sphere size, matrix material and processing technique.

5. Experimental evaluation of mechanical properties of composite metal foams and optimization of the properties of Composite Metal Foams for nuclear application.

<u>Main achievements:</u>

Publications:

- Shuo Chen, Jacob Marx, Afsaneh Rabiei, "Experimental and computational studies on the thermal behavior and fire retardant properties of composite metal foams", International Journal of Thermal Sciences. Accepted with minor revision.
- Shuo Chen, Jacob Marx, Afsaneh Rabiei, "Experimental and computational studies on the thermal behavior of composite metal foams under extreme heat conditions", 9th International Conference on Porous Metals and Metallic Foams, MetFoam, Barcelona, Spain, August 31-September 2, 2015. This paper is currently in review for publication.
- Shuo Chen, Mohamed Bourham, Afsaneh Rabiei, "Attenuation efficiency of X-ray and comparison to gamma ray and neutrons in composite metal foams", Radiation Physics and Chemistry, 117, pp. 12-22, 2015. *This paper has been announced as the top three papers downloaded from the science direct in 2015: (http://www.journals.elsevier.com/radiation-physics-and-chemistry/most-downloaded-articles/).*
- Shuo Chen, Mohamed Bourham, Afsaneh Rabiei, "Neutrons attenuation on composite metal foams and hybrid open-cell Al foam", Radiation Physics and Chemistry, 109, pp. 27-39, 2015. *This paper was also ranked as one of the top 20 highly viewed articles from Science Direct and has been viewed 581 times within the first year after publication.*
- Shuo Chen, Mohamed Bourham, Afsaneh Rabiei, "Applications of open-cell and closed-cell metal foams for radiation shielding", Procedia Materials Science, 4, pp. 293-298, 2014.
- Shuo Chen, Mohamed Bourham, Afsaneh Rabiei, "A novel light-weight material for shielding gamma ray", Radiation Physics and Chemistry, 96, pp. 27-37, 2014.

Presentations:

- Afsaneh Rabiei, "Overview of Composite Metal Foams and Metallic Bubble Wraps from Inception Till Now" a keynote presentation in August 2015.
- Shuo Chen, Afsaneh Rabiei, "Experimental and computational studies on the thermal behavior of composite metal foams under extreme heat conditions" 9th International Conference on Porous Metals and Metallic Foams, MetFoam poster presentation in August 2015
- Shuo Chen, Mohamed Bourham, Afsaneh Rabiei, "Applications of open-cell and closed-cell metal foams for radiation shielding", Oral presentation by Shuo Chen in 8th international conference on porous metals and metallic foams, MetFoam, Raleigh, NC, June 23-26, 2013.
- Afsaneh Rabiei, "New Discoveries on Metal Foams & Their Potentials" Key note presentation in 8th International Conference on Porous Metals and Metallic Foams, MetFoam, Raleigh, NC, June 23-26, 2013.
- Afsaneh Rabiei, "Processing and Properties of porous composite metal foams" Key note presentation in 4th International Conference on Porous Media and its Applications in Science, Engineering and Industry, June 17-22, 2012 Potsdam, Germany.

Timeline:

- The PhD student who has been working on this project is graduated in August 2015.

CHAPTER 2 INTRODUCTION

Radiation shielding materials are commonly used in nuclear facilities to attenuate the background ionization radiations to a minimum level for creating a safer workplace, meeting regulatory requirements and maintaining high quality performance. The conventional radiation shielding materials have a number of drawbacks: heavy concrete contains a high amount of elements that are not desirable for an effective shielding such as oxygen, silicon, and calcium [1]; a well known limitation of lead is its low machinability and toxicity, which is causing a major environmental concern. Therefore, an effective and environmentally friendly shielding material with increased attenuation and low mass density is desirable.

Close-cell composite metal foams (CMFs) and open-cell Al foam with fillers are lightweight candidate materials that we have studied in this project. Close-cell CMFs possess several suitable properties that are unattainable by conventional radiation shielding materials such as low density and high strength for structural applications, high surface area to volume ratio for excellent thermal isolation with an extraordinary energy absorption capability [2, 3]. Open-cell foam is made up of a network of interconnected solid struts, which allows gas or fluid media to pass through it [4]. This unique structure provided a further motive to investigate its application as radiation shields by infiltrating original empty pores with high hydrogen or boron compounds, which are well known for their excellent neutron shielding capability. The resulting open-cell foam with fillers will not only exhibit lightweight and high specific surface area, but also possess excellent radiation shielding capability and good processability [5].

In this study, all the foams were investigated for their radiation shielding efficiency in terms of X-ray, gamma ray and neutron. X-ray transmission measurements were carried out on a high-resolution microcomputed tomography (microCT) system. Gamma-emitting sources: 3.0mCi ^{60}Co, 1.8mCi ^{137}C$_S$, 13.5mCi ^{124}Am, and 5.0mCi ^{133}Ba were used for gamma-ray attenuation analysis. The evaluations of neutron transmission measurements were conducted at the Neutron Powder Diffractometer beam facility at North Carolina State University. The experimental results were verified theoretically through XCOM and Monte Carlo Z-particle Transport Code (MCNP).

A mechanical investigation was performed by means of quasi-static compressive testing. Thermal characterizations were carried out through effective thermal conductivity and thermal

expansion analyses in terms of high temperature guarded-comparative-longitudinal heat flow technique and thermomechanical analyzer (TMA), respectively. The experimental results were compared with analytical results obtained from respectively Brailsford and Major's model and modified Turner's model for verification. Flame test was performed in accordance with United States Nuclear Regulatory Commission (USNRC) standard. CMF sample and a 304L stainless steel control sample were subjected to a fully engulfing fire with an average flame temperature of 800°C for a period of 30 minutes. Finite Element Analysis was conducted to secure the credibility of the experimental results.

This research indicates the potential of utilizing the lightweight close-cell CMFs and open-cell Al foam with fillers as shielding material replacing current heavy structures with additional advantage of high-energy absorption and excellent thermal characteristics.

CHAPTER 3   MATERIALS PROCESSING AND CHARACTERIZATION

Aluminum A356 alloy was chosen as reference material in this study. Total twelve sets of samples were designed and tested to evaluate their shielding capabilities against X-ray, gamma ray and thermal neutrons:

- Composite metal foams with 2mm steel hollow spheres and Aluminum A356 matrix [(2mm sphere) Al-S CMFs]
- Composite metal foams with 4mm steel hollow spheres and Aluminum A356 matrix [(4mm sphere) Al-S CMFs]
- Composite metal foams with 5.2mm steel hollow spheres and Aluminum A356 matrix [(5.2mm sphere) Al-S CMFs]
- Composite metal foams with 2mm steel hollow spheres and 316L stainless steel matrix [(2mm sphere) S-S CMFs]
- Composite metal foams with 4mm steel hollow spheres and 316L stainless steel 316L matrix [(4mm sphere) S-S CMFs]
- Composite metal foams with 5.2mm steel hollow spheres and 316L stainless steel matrix [(5.2mm sphere) S-S CMFs]
- Composite metal foams with 4mm steel hollow spheres and a mixture of 316L stainless steel matrix and high-speed T15 steel containing high-Z elements [(4mm sphere) HZ S-S CMFs]
- Aluminum A356 (control sample)
- Open-cell Al foam + paraffin wax, sandwich composite (Open-cell Al foam + wax)
- Open-cell Al foam + borated polyethylene, sandwich composite (Open-cell Al foam + PE)
- Open-cell Al foam + water, sandwich composite (Open-cell Al foam + water)
- Open-cell Al foam + borated water, sandwich composite (Open-cell Al foam + borated water)

3.1   Materials and Sample Preparation

3.1.1   Composite Metal Foam Samples

A New Light Weight Structural Material for Nuclear Structures

Aluminum A356 casting alloy (TriAlCo, Inc), stainless steel hollow spheres (Hollomet GmbH, Dresden, Germany), and 316L stainless steel powder (North American Hoganas High Alloys LLC) with particle size sieved to -325 mesh (95%) and -200/+325 mesh (5%) were used in processing of close-cell CMFs. Three sizes of hollow spheres with outer diameters of 2.0, 4.0, and 5.2mm were used for manufacturing close-cell CMFs. Elemental compositions of hollow spheres are shown in Table 3–1 and Table 3–2: as well as compositions of both aluminum A356 casting alloy and 316L stainless steel powder used as the matrix materials.

Table 3–1: Chemical compositions of different spheres in close-cell CMFs (wt%)

	2.0mm diameter	4.0mm diameter	5.2mm diameter
C	0.68	0.58	0.87
Mn	0.13	0.15	0.07
Si	0.82	1.14	0.34
Cr	16.11	17.34	17.09
Ni	11.53	12.28	12.60
Mo	2.34	2.28	2.12
P	--	0.009	--
S	--	<0.003	--
Cu	--	0.04	--
Co	--	0.02	--
Fe	balance	balance	balance

Steel-steel CMF and Al-steel CMF consist of a random dense arrangement of steel hollow spheres surrounded by a metallic matrix. Steel-steel CMF samples were processed by a PM technique. Both spheres and steel powder were placed into a mold and vibrated at frequency of 20Hz for approximately 50min to achieve dense packing between the spheres and matrix. The samples were then sintered at 1200- 1250°C in a vacuum hot press. More details on processing CMF by PM technique can be found elsewhere [3, 6, 7, 8]. Al-steel CMF samples were processed by gravity casting. The hollow spheres were placed into a mold and pre-heated to 700°C in a high temperature furnace. Molten Al (also heated to 700°C) is then cast into the mold

and the sample is allowed to cool at room temperature. More details of processing CMF through casting methods can be found elsewhere [9, 10, 11, 12].

Table 3–2: Chemical compositions of matrix in close-cell CMFs (wt%)

	316L stainless steel	High-speed T15 steel	Aluminum A356.2
C	0.03	1.60	--
Mn	2.00	0.40	0.28
Si	1.00	≤0.40	7.01
Cr	16.00-18.00	4.00	0.02
Co	--	5.00	--
Ni	10.00-14.00	--	--
Mo	2.00-3.00	≤1.00	--
P	--	--	--
S	--	0.04	--
Cu	--	--	0.11
Fe	balance	balance	0.50
Mg	--	≤0.40	0.39
Ti	--	--	0.09
Zn	--	--	0.06
Al	--	--	balance
W	--	12.50	--
V	--	5.00	--

All samples have been designed to have the same cross sectional area for testing (rectangular area 50.8mm x 89.3mm), and sample thickness is varied according to the areal density. Samples of each material were made with three different areal densities of 2, 5 and 10g/cm². Digital images and cut sections for close-cell CMF samples are shown in Figure 3–1 and Figure 3–2. Measured dimensions and mass were used to calculate the volumetric density and the areal density of each sample. Physical properties of close-cell CMFs and open-cell Al foam with fillers are presented in Table 3-3.
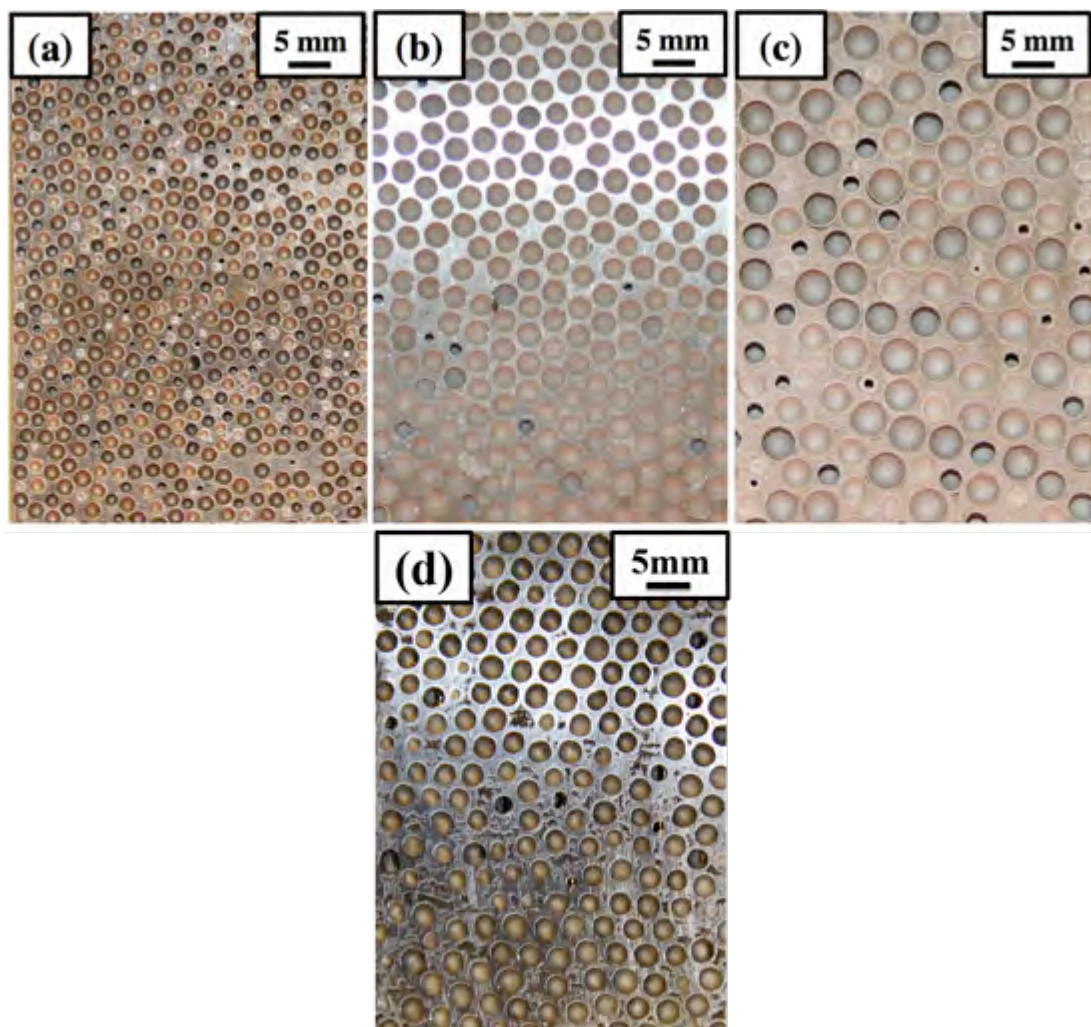
Figure 3–1: Digital images showing cross-sectional areas of (a) (2mm sphere) S-S CMF, (b) (4mm sphere) S-S CMF, (c) (5.2mm sphere) S-S, and (d) (4mm sphere) HZ S-S CMF
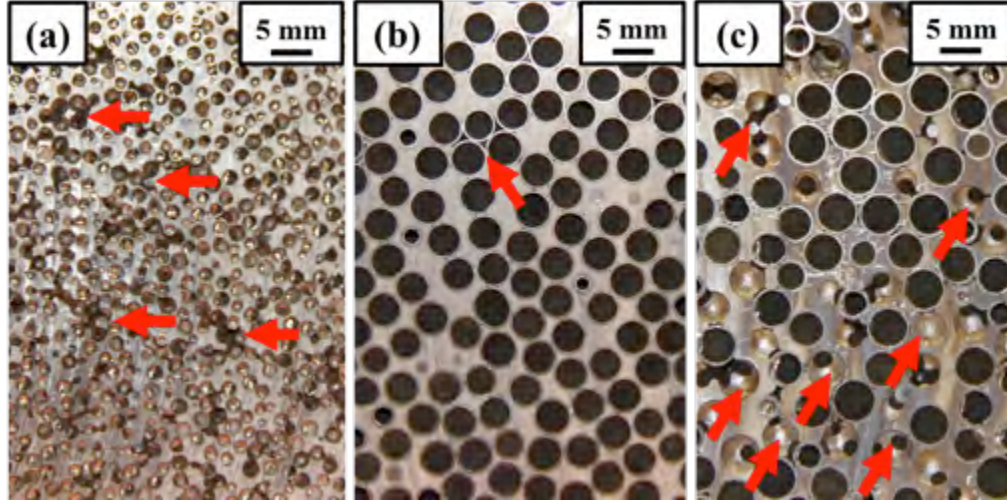
Figure 3–2: Digital images showing Al-steel CMFs produced with (a) 2.0mm, (b) 4.0mm and (c) 5.2mm spheres with Aluminum A356 matrix. Arrows show some defects in the sample due to processing and are inevitable in cast CMFs

Thickness of each composite foam sample (T_{CMF}) required to have an areal density (ρ_A) of 2, 5 and 10g/cm^2 was calculated by considering the bulk density of the composite foam (ρ_{CMF}) and the area of the test section (A_{test}) as shown in Eq. (1):

$$\rho_A = mass / area = A_{test} T_{CMF} \rho_{CMF} / A_{test} \tag{9}$$

Rearranging Eq. (9) to solve for the required thickness gives Eq. (10) shown below. Density values used in this calculation are an average from several samples and are equal to 2.70g/cm^3 for steel-steel CMF and 2.03g/cm^3 for Al-steel CMF.

$$T_{CMF} = \rho_A / \rho_{CMF} \tag{10}$$

Table 3–3: Physical properties of close-cell CMFs and Aluminum A356

	Designed areal density (g/cm²)	Thickness (cm)	Volumetric density (g/cm³)	Measured areal density (g/cm²)	Difference of designed and measured areal density (%)
(2.0mm) Steel-steel CMF	2	0.77	2.50	1.93	-3.61
	5	1.91	2.50	4.78	-4.40
	10	4.03	2.36	9.50	-5.05
(2.0mm) Al-steel CMF	2	1.08	1.90	2.05	2.59
	5	2.62	1.97	5.17	3.48
	10	5.19	1.91	9.90	-0.98
(4.0mm) Steel-steel CMF	2	0.72	2.70	1.94	-2.79
	5	1.75	2.83	4.97	-0.58
	10	3.69	2.73	10.06	0.58
(4.0mm) Al-steel CMF	2	1.00	1.91	1.92	-4.05
	5	2.43	2.00	4.88	-2.39
	10	4.92	1.92	9.42	-5.77
(5.2mm) Steel-steel CMF	2	0.79	2.63	2.09	4.50
	5	1.81	2.71	4.91	-1.8
	10	3.65	2.71	9.91	-0.90
(5.2mm) Al-steel CMF	2	1.11	1.79	1.99	-0.50
	5	2.60	1.89	4.91	-1.80
	10	5.33	1.99	10.61	6.10
Aluminum A356	2	0.74	2.72	2.01	0.28
	5	1.86	2.70	5.03	0.66
	10	3.72	2.70	10.04	0.41

3.1.2 Open-Cell Al Foam with Filler Samples

In open-cell Al foam with fillers, the samples are contained inside a custom built box constructed from 6061 Al alloy seamless tubing (101.6mm x 101.6mm outer dimensions, 6.13mm wall thickness). The general design for these boxes is shown in Figure 3–3.
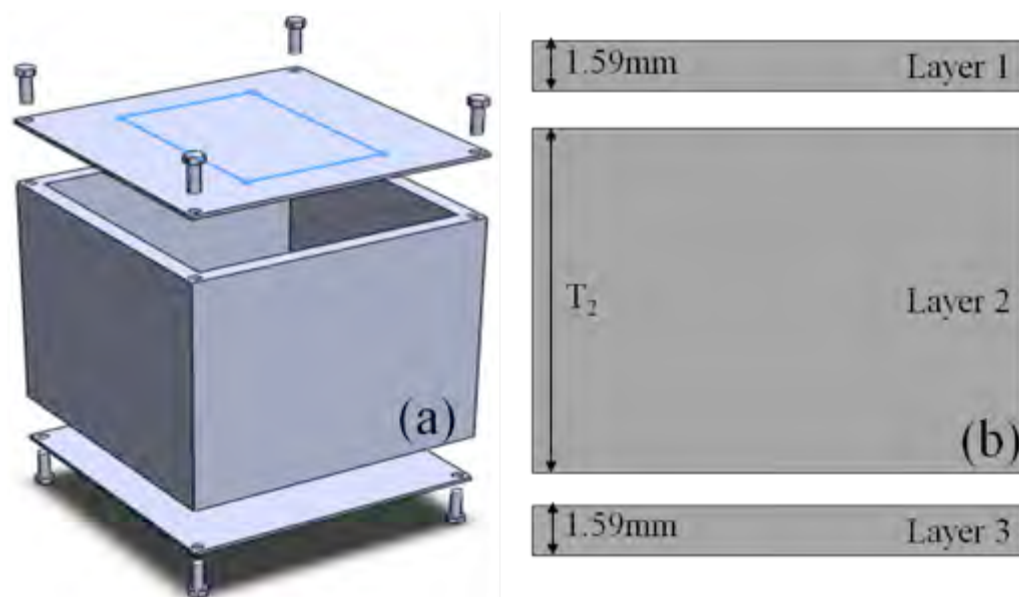
Figure 3–3: (a) Al container box. The interior of the box will be filled with the Layer 2 composite material. Box height shown is representative of a sample with areal density of 10 g/cm^2, (b) Cross section view of sample test section

The top and bottom face sheets correspond to Layer 1 and Layer 3 of the sample and are secured to the tubing with screws and sealant glue to prevent any filler leakage. Dimensions of the tubing cross section were chosen to facilitate simple manufacturing by allowing off-the-shelf components to be used since the box walls serve only as a container. Layers 1 and 3 are Al face sheets with 1.59mm thickness and a composition as shown in Table 3–4. Layer 2 is a composite made from open-cell Al foam infiltrated with an additional filler material: petroleum wax, borated polyethylene, or water (composition shown in Table 3–4). The thickness of the Layer 2 is dictated by the areal density requirements and varies for each sample.

Table 3–4: Chemical compositions of 6061 Al alloy face sheet and open-cell Al foam (wt %)

	6061 Al alloy face sheet	Open-cell Al foam
B	--	≤ 0.060
Cr	0.04-0.35	≤ 0.030
Cu	0.15-0.40	≤ 0.10
Fe	≤ 0.70	≤ 0.50
Mg	0.80-1.20	0.35-0.80
Mn	≤ 0.15	≤ 0.030
Si	0.40-0.80	0.30-0.70
Ti	≤ 0.15	--
Zn	≤ 0.25	≤ 0.10
other	≤ 0.15	≤ 0.10
Al	95.8-98.6	≥ 97.6

Table 3–4: Chemical compositions of filler materials (wt %)

	Petroleum wax	Borated polyethylene	Water	Borated water
H	14.8	11.6	11.2	11.1
B	--	5.0	--	0.2
C	85.2	61.2	--	--
O	--	22.2	88.8	88.7

The open-cell Al foam is manufactured from Al 6101-T6 alloys (ERG Aerospace Corporation) and has approximately 5 pores per linear inch. Elemental composition of the foam ligament material is shown in 3–4. The three types of filler materials are petroleum wax (IG Wax), borated polyethylene (5wt% boron, Shieldwerx), and water. Composition of the polyethylene is 11.60wt% H, 61.20wt% C, 22.20wt% O, and 5wt% B. The petroleum wax is composed of carbon and hydrogen polymer chains that follow the chemical formula C_nH_{2n+2}.

Figure 3–4 shows digital image of the open-cell Al foam with filler samples after Layer 2 has been manufactured but before the boxes was completely sealed. A 50.8mm x 89.3mm test section is marked on the center of the box to match the size of the composite metal foam samples, as well as to avoid the edge effect during testing. For the samples with petroleum wax and

borated polyethylene filling, Layer 2 was manufactured by infiltrating the open-cell Al foam with melted filler material inside the Al tubing box. First the weight of the empty box body without any face sheets, hardware, or filler was recorded. The open-cell Al foam portion of Layer 2 was inserted into the box, and the lower face sheet (Layer 3) was fastened to the box body with removable screws. The partial assembly was then heated on a hot plate while the filler material was melted in a separate container. Heating temperatures of the filler were 120°C for the borated polyethylene and 100°C for the petroleum wax. The filler material was then poured slowly into the heated box until no more air bubbles were observed escaping from inside the foam porosities and the filler no longer sank down into the sample. The samples were then allowed to air cool to room temperature.
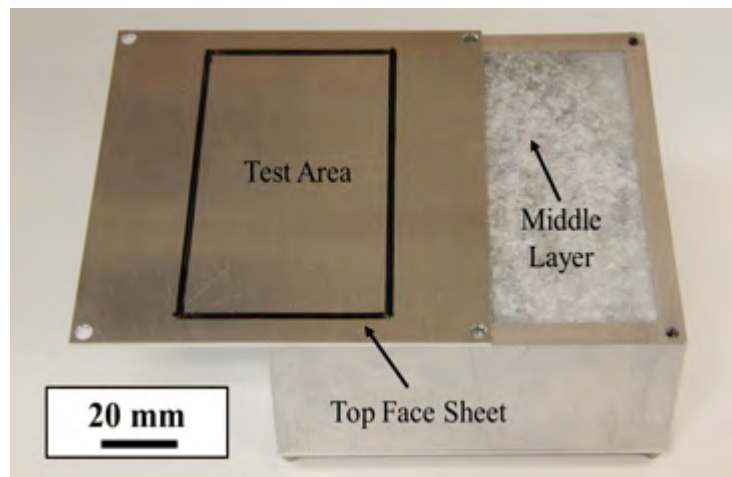
Figure 3–4: Digital images showing open-cell Al foam + PE at areal density of 5g/cm^2, with removable top face sheet and a middle layer infiltrated with PE

Layer 1 was then screwed in, the sample is flipped and layer 3 is removed to inspect the lower surface of the sample to make sure the filler had completely filled all porosities in layer 2. Weight of the box body/Al foam/filler assembly was recorded and then the face sheets (Layer 1 and Layer 3) were secured in place with sealant glue and screws.

For the samples with water filling, no heating was necessary as the water could easily fill the porosities at room temperature. The open-cell Al foam was inserted into the box, the bottom face sheet (Layer 3) was fully sealed onto the bottom of the box, and the sample was then filled with the water. The top face sheet (Layer 1) was then sealed onto the upper surface of the box. These samples were also weighed before and after filling.

A New Light Weight Structural Material for Nuclear Structures

The thickness of Layer 2 required obtaining areal densities of 2, 5 and 10g/cm^2 for each filler material were calculated by considering the cross section in the 50.8mm x 89.3mm test area of the sample (Figure 3–4). The areal density of the whole composite (ρ_A) is equal to the total mass of material in this region divided by the cross sectional area (A_{test}), where the total mass is equal to the sum of each layer as shown in Eq. (11). Since Layer 1 and Layer 3 are made from the same material and are the same thickness, it is assumed that their masses are equal ($m_1 = m_3$). The total mass of Layer 2 is equal to the sum of the open-cell Al foam ligaments mass and the filler material mass.

$$\rho_A = mass \, / \, area = \left(2m_1 + m_{foam} + m_{filler}\right) / A_{test} \tag{11}$$

Each layer mass is then written in terms of its volume and density in order to calculate the areal density of the whole composite in terms of the densities of its components (Eq. 11). The density of each filler material was measured experimentally and is shown in Table 3–5, while the density of Layer 1 and Layer 3 was taken to equal that of bulk Al (2.7g/cm^3).

Relative density of the open-cell Al foam was determined to be 5% by comparing the measured density to that of bulk Al. Consequently, 5% of the total foam volume is occupied by the Al ligaments, and 95% of the total foam volume is occupied by filler material inside the pores.

$$\rho_A = \left[2(A_{test}T_1)\rho_{Al} + 0.05(A_{test}T_2)\rho_{Al} + 0.95(A_{test}T_2)\rho_{filler}\right] / A_{test} \tag{12}$$

Eq. (12) can be simplified since the cross section area (A_{test}) is common to all terms. After simplification and re-arranging, Eq. (12) is solved for the thickness of Layer 2 (T$_2$) needed to produce a specific areal density. This is shown below in Eq. (13):

$$T_2 = \left(\rho_A - 2T_1\rho_{Al}\right) / \left(0.05\rho_{Al} + 0.95\rho_{filler}\right) \tag{13}$$

Areal density of the material occupying the box interior was calculated from the measured weights of the samples before and after filling Layer 2. The mass of Layer 1 and Layer 3 was calculated from the known sheet thickness, interior box dimensions, and the density of bulk Al (2.7g/cm^3). The mass of Layer 2 was obtained by subtracting the mass of the empty box from the mass of the box after filling, as given by Eq. (14):

$$m_2 = m_{foam} + m_{filler} = m_{filled\_box} - m_{empty\_box} \tag{14}$$

The measured areal density is then calculated by adding the mass of each layer together and dividing by the area of the box interior (Eq. 12). These values are shown in Table 3–5 with a comparison to the designed areal density.

Table 3–5: Physical properties of open-cell Al foam with fillers

	Designed areal density (g/cm²)	Thickness (cm)	Volumetric density (g/cm³)	Measured areal density (g/cm²)	Difference of designed and measured areal density (%)
Open-cell Al foam + Wax	2	1.54	1.31	1.32	1.96
	5	4.74	1.15	1.05	-0.98
	10		1.05	0.98	-1.23
Open-cell Al foam + PE	2	1.49	1.32	1.31	-2.49
	5	4.57	1.05	1.15	5.08
	10	9.69	0.98	1.03	-0.27
Open-cell Al foam + Water	2	1.37	1.35	1.84	-7.80
	5	4.14	1.20	4.98	-0.35
	10	8.77	1.15	10.05	0.53
Open-cell Al foam + Borated Water	2	1.37	1.35	1.84	-7.80
	5	4.14	1.20	4.98	-0.35
	10	8.77	1.15	10.05	0.53

3.2 Characterization

Samples for optical and scanning electron microscopy (SEM) analysis were prepared using a Buehler Isomet 4000 precision cutting saw. Thin slice of close-cell CMF samples were cut with a wafering blade rotating at a rate of 2500 rpm and 1.0 mm feeding rate. These samples were surfaced using Buehler Automet 2 Power Head grinding and polishing stations. Grinding was conducted using a progression of 240, 600, 1200, and 4000 grit papers at a wheel speed of 90 rpm for steel-steel CMFs and 70 rpm for Al-steel CMFs. Each sample was then polished with 3μm diamond slurry, and followed by 1, 0.3, and 0.05μm alumina paste, using a wheel speed of 120rpm for steel-steel CMFs and 70rpm for Al-steel CMFs. Buehler Unimet Unitron 9279 microscope equipped a Hitachi KP-M1 CCD digital camera was utilized to obtain optical microscopy images in order to evaluate the microstructure of the sphere and matrix. SEM analysis was performed using Hitachi S-3200N environmental SEM equipped with EDX in order to investigate the more detailed microstructure of samples.

CHAPTER 4   EXPERIMENTS

4.1   X-Ray Transmission Measurements

A high-resolution microcomputed tomography (microCT) system (eXplore speCZT CT 120, TriFoil Imaging, Inc. Chatsworth, CA), shown in Figure 4–1, was used to acquire X-ray projection images of close-cell CMFs, Aluminum A356 and lead. The X-ray source is a high power rotating-anode tube with the capability of running under variable energy and current at the focal spot size of 600 um. In this study, the source was operated at maximum energy of 100 kVp, current of 50mA, exposure time of 20ms, and binning mode under 2x2. The CCD flat panel detector is comprised of 3500x2288 pixel elements covering an active area of 110x75mm^2. The source and the detector positioning opposite to each other were set at a fixed distance of 450 mm. During each measurement, the source and the detector move on a circular trajectory around a fixed carbon fiber tube sitting in the center point. Both the experimental sample and the control materials: Aluminum A356 and lead were placed inside the tube under the same field of view at each measurement. The data acquisition time was 2.5 sec per projection, and the images were formed from 360 views taken over a 360^0 rotation. The Feldkamp's filtered back projection algorithm was used to reconstruct projection images with resolution of 50um.

Figure 4–1: Microcomputed tomography (microCT) system

4.2   Gamma-ray Transmission Measurements
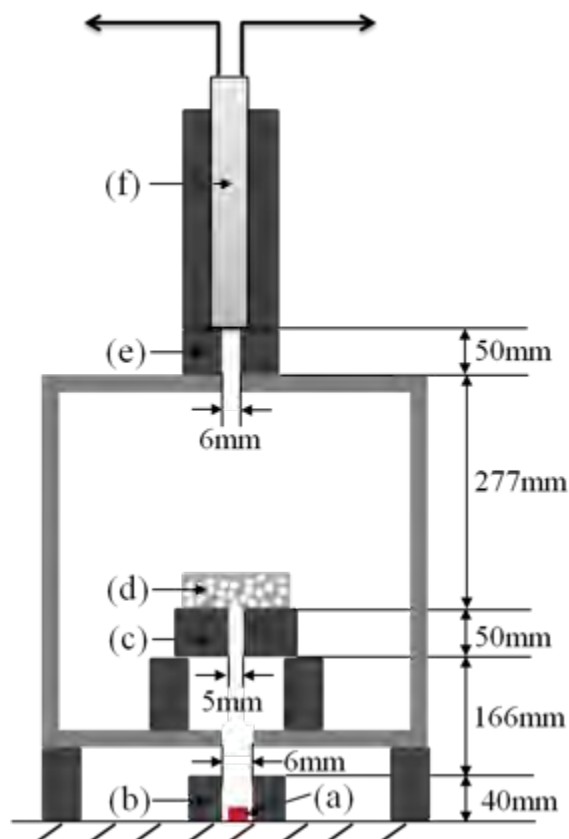
Figure 4–2: Schematic diagram of gamma spectrometry system with (a) gamma ray source, (b) source collimator, (b) sample collimator, (d) detector collimator, and (e) NaI detector

The gamma ray attenuation experiments were performed in vertical narrow beam transmission geometry. The gamma detection apparatus is displayed in Figure 4–2. The distance between the radioactive source and detector was 583mm and the source was collimated using a lead holder with a collimating rectangular hole of 8mm x 23mm to obtain a narrow parallel beam. The sample was placed onto a sample collimator at a distance of 256mm from the source; thereafter the photon flux leaving the sample was allowed to pass through a detector collimator before reaching the detector. The sample and the detector collimators with a central hole of 6mm and 5mm respectively were used to minimize the detection of any scattered photons coming directly from the source and the surroundings. The 2in.x2in sodium iodide (NaI) detector (ORTEC model 905-3) was mounted on to a preamplifier (ORTEC model 266), and surrounded by a lead shield in order to decrease the detection of any accidental signals. The whole detection system was held on a steel frame. The output from the preamplifier was coupled to a multi-

channel analyzer (ORTEC model 575A), which provided signals to a PC using Canberra Genie 2000 as the software platform for gamma acquisition and analysis. The vertical linearity of the symmetry axis of the arrangement was adjusted using a laser pointer. The gamma ray spectrum was acquired for a constant count of 200,000 for each measurement, which was reasonable enough to obtain a statistical uncertainty in the range of 0.21% to 0.62%. Each sample was measured with photon energies of 0.06, 0.662, 1.173, and 1.332MeV, respectively. The sample was interposed in the beam and counting experiments were conducted to measure the attenuated beam intensity. Following that, the sample was removed in order to measure the unattenuated beam. Three consecutive measurements were undertaken for each sample at the set energy values and the average of the three was used in actual calculations.

4.3   Thermal Neutron Transmission Measurements
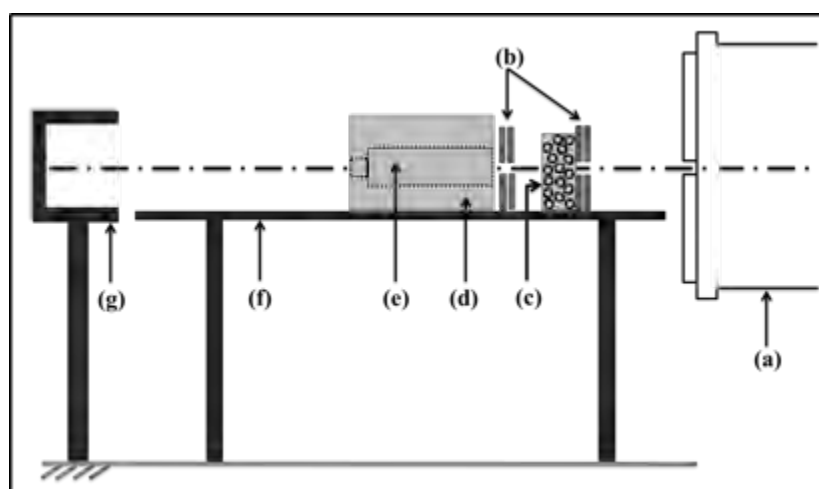
Figure 4–3: Experimental geometry for neutron spectrometry system with (a) neutron beam, (b) Cd collimators, (c) sample, (d) B$_4$C detector shielding, (e) BF^3 neutron detector, (f) Al supporting table, (g) neutron beam shielding

Neutron transmission measurements were carried out using the Neutron Powder Diffractometer beam available at North Carolina State University PULSTAR nuclear reactor [13]. At this facility, the thermal neutron intensities of approximately 2.7×10^{12} n/cm^2/s is obtained at the entrance of beam tube #4 and approximately 0.64×10^5 n/cm^2/s at the guide aperture with a reactor power of 1 MW. The beam is monochromatic and comprised of 0.035eV neutrons with a single energy correlating to a wavelength of 1.5 angstroms. The general experimental arrangement is shown in Figure 4–3.

A New Light Weight Structural Material for Nuclear Structures

The whole detection system was held on an Aluminum 6061 table 83cm from the floor. The sample was placed at 36cm downstream from the guide aperture to allow for the greatest possible neutron flux. The neutron beam was limited to be 1.3cm in diameter by stacking of two Cd collimators with dimensions of $20 \times 20 \times 1 cm^3$, another two stacking collimators with the same dimensions were placed 22cm downstream from the sample. These four collimators provide specific intensity and geometry to the neutron beam, meanwhile, eliminating the side scattered radiation from the beam line and enhancing its discrimination capability. A BF_3 detector (GE-Reuter Stokes model RS-P1-1506-202) was inserted into a B_4C shield tube, which was used to decrease the counting of unwanted background radiation. The detector is 5cm in diameter by 46cm long. The filled gas is BF_3, with 90% ^{10}B enrichment at a pressure of 20cm Hg. The detection system was placed 3cm downstream from the fourth Cd plate perpendicularly to the beam axis. The detector was mounted onto a preamplifier (ORTEC Model 142PC) and the output from the preamplifier was coupled to an amplifier (ORTEC Model 575), which provided signals to integral discriminator (ORTEC Model 421) to cut off low energy background peaks. The transmitted number of neutrons was displayed on the Timer and Counter (ORTEC Model 871). The detector and its electronics linearity was tested and checked before the course of experimental measurements by measuring the detector count rate at reactor power at every 100kW intervals from 1 to 10^3 kW. The data shows excellent linearity and stability. The transmitted (Φ_{mt}) neutron intensities were recorded in a 600s interval, which was reasonable enough to obtain a statistical uncertainty in the range of 0.42% to 0.47%. Statistical uncertainty was determined by $1/\sqrt{N}$ (N is number of counts). The background radiation (Φ_{mb}) was subtracted from each measurement to correct for the contribution of nuclear radiation from some extraneous sources at PULSTAR reactor (i.e., Neutron Imaging source at beam tube #5, and Intense Positron source at beam tube #6), or radiation from the environment (cosmic rays, building materials, etc). The background measurement was conducted by placing a 5cm thick paraffin brick at the sample position, and recorded in a 600s interval. The neutron transmission was calculated using Equation (6) after acquiring the corresponding open beam (Φ_{mo}) at a constant time of 10s. Open beam was counted repeatedly between each sample measurement within a very stable error of ±2%, therefore, all the measurements were performed without a beam-monitoring detector. Experimental results were compared with theoretical values calculated by MCNP5 developed at the Los Alamos National Laboratory.

4.4   Quasi-static Compression Test

Two types of cylindrical samples, (4mm sphere) S-S CMFs and (4mm sphere) HZ S-S CMFs were prepared for quasi-static compression test. Figure 4–4a shows the digital image of compression test samples after sintering. Each cylindrical sample (25mm in diameter) was cut into three small pieces (top, middle, and bottom) using a precision saw equipped with a diamond-wafering blade. As illustrated in Figure 4–4b, each small piece has a height of 25mm, giving a height/diameter ratio of 1.

In order to fully understand the feasibility of utilizing HZ S-S CMFs as structural material in nuclear application, exploring their mechanical properties under loading and resulted total energy absorption capability is of crucial importance. For this purpose, the mechanical performance of HZ S-S CMFs under quasi-static compression was performed and compared to that of other classes of S-S CMF materials.

Quasi-static compression tests were conducted using an MTS 810 universal testing machine with a 980kN load cell and a crosshead speed of 1.25 mm/min (Neville and Rabiei, 2008) at Construction Facilities Laboratory (CFL) at North Carolina State University. A digital camera (Canon, EOS 7D) was employed to observe the samples' deformation under compression loading. Vacuum grease was applied to both ends of each testing samples in order to lubricate the contact surfaces between the samples and the testing machine to minimize friction and resulted barreling effects. Each measurement was repeated three times. Collected data were treated to obtained stress-strain curve.
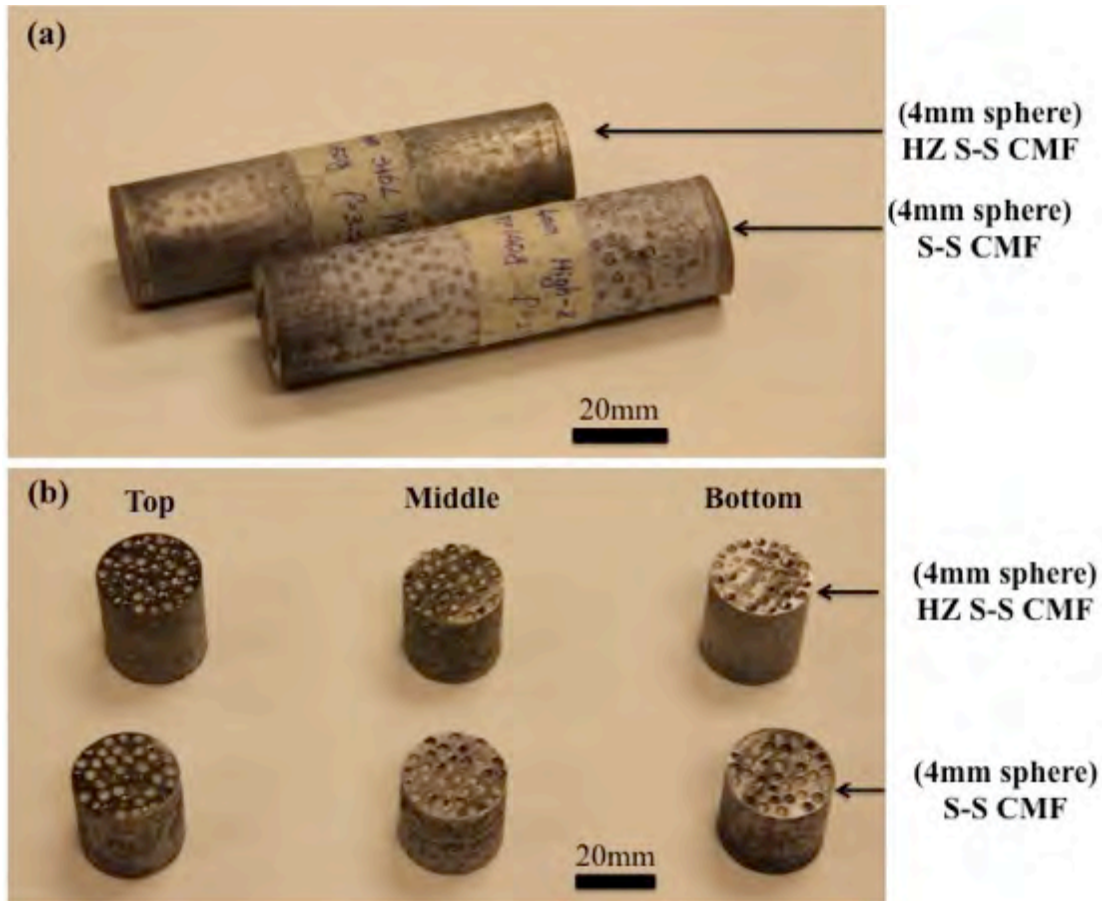
Figure 4–4: Compression test samples (a) before, and (b) after cutting

4.5 Thermal Analysis

In the nuclear facilities, materials are often subjected to high temperature, which leads to the interest in their thermal properties investigation, such as effective thermal conductivity, coefficient of thermal expansion, and their flame resistant.

4.5.1 Effective Thermal Conductivity Analysis

Three CMF samples of nominal dimensions 2.54x2.54x2.54cm were prepared for effective thermal conductivity measurements:

- (2mm sphere) S-S CMF

- (4mm sphere) S-S CMF

- (4mm sphere) Al-S CMF

A New Light Weight Structural Material for Nuclear Structures

These samples were designed to study the effect of sphere size and matrix material on thermal conductivity of CMFs and compared with the properties of 316L stainless steel and Aluminum A356 available in literature. The specimen ends (top and bottom surfaces as illustrated in Figure 4–5) were prepared to be flat and parallel to each other, and perpendicular to the sides within 0.001 inch per inch. The surfaces were then finished using a progression of 240, 600, and 1200 grit sand papers at a wheel speed of 90rpm for S-S CMFs and 70rpm for Al-S CMFs, in order to improve the flatness, parallelism and thickness uniformity. Physical properties of the samples are summarized in Table 4–1.
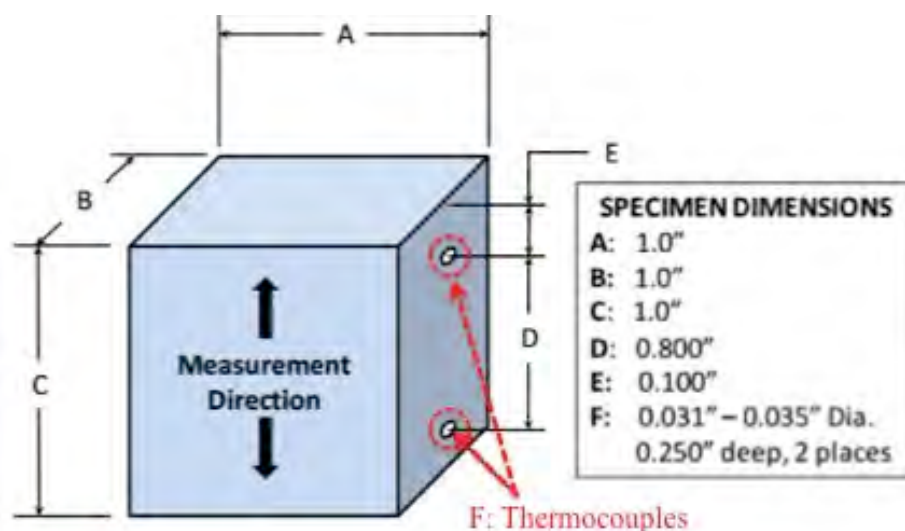
Figure 4–5: Dimensions of thermal conductivity specimen, dashed circles indicate the positions for thermocouples

Table 4–1: Physical properties of CMFs for effective thermal conductivity measurements

Samples	Thickness (cm)	Width (cm)	Length (cm)	Volumetric Density (g/cm^3)
(2mm sphere) S-S CMF	2.54	2.54	2.54	2.7
(4mm sphere) S-S CMF	2.54	2.54	2.54	2.6
(2mm sphere) Al-S CMF	2.54	2.54	2.54	1.9

The effective thermal conductivities of (2mm sphere) S-S CMF, (4mm sphere) S-S CMF, and (4mm sphere) Al-S CMF were measured by means of high temperature guarded-comparative-longitudinal heat flow technique (Testing service provided by Precision Measurements and Instruments Corporation (PMIC)). The measurement system design was adapted from the American Society of Testing and Materials (ASTM) E1225-04 as shown schematically in Figure 4–6.

In this technique, CMFs of unknown thermal conductivity was inserted between two stainless steel meter bars of known thermal conductivity forming a sample stack. 1/8" thick copper shims were placed between the specimen and meter bars to act as lateral heat spreaders. 0.020" diameter metal-sheathed K-type thermocouples were used for temperature measurement. Six thermocouples were embedded in the appropriate holes at specific locations to record the temperature along the axial direction during the heating process. As indicated in Figure 4–6a, the thermocouples were located 0.1" apart from the top and bottom surfaces of specimen and meter bars. The temperature values were continuously recorded as a function of time using a Labview-based program on a PC workstation. A small quantity of thermal grease was applied to the tip of each thermocouple to improve thermal grounding to the specimen or meter bars. A thin film of thermal grease was also applied at each interface, between the specimen, copper shims, meter bars and hot and cold plates to reduce or eliminate the thermal resistance.
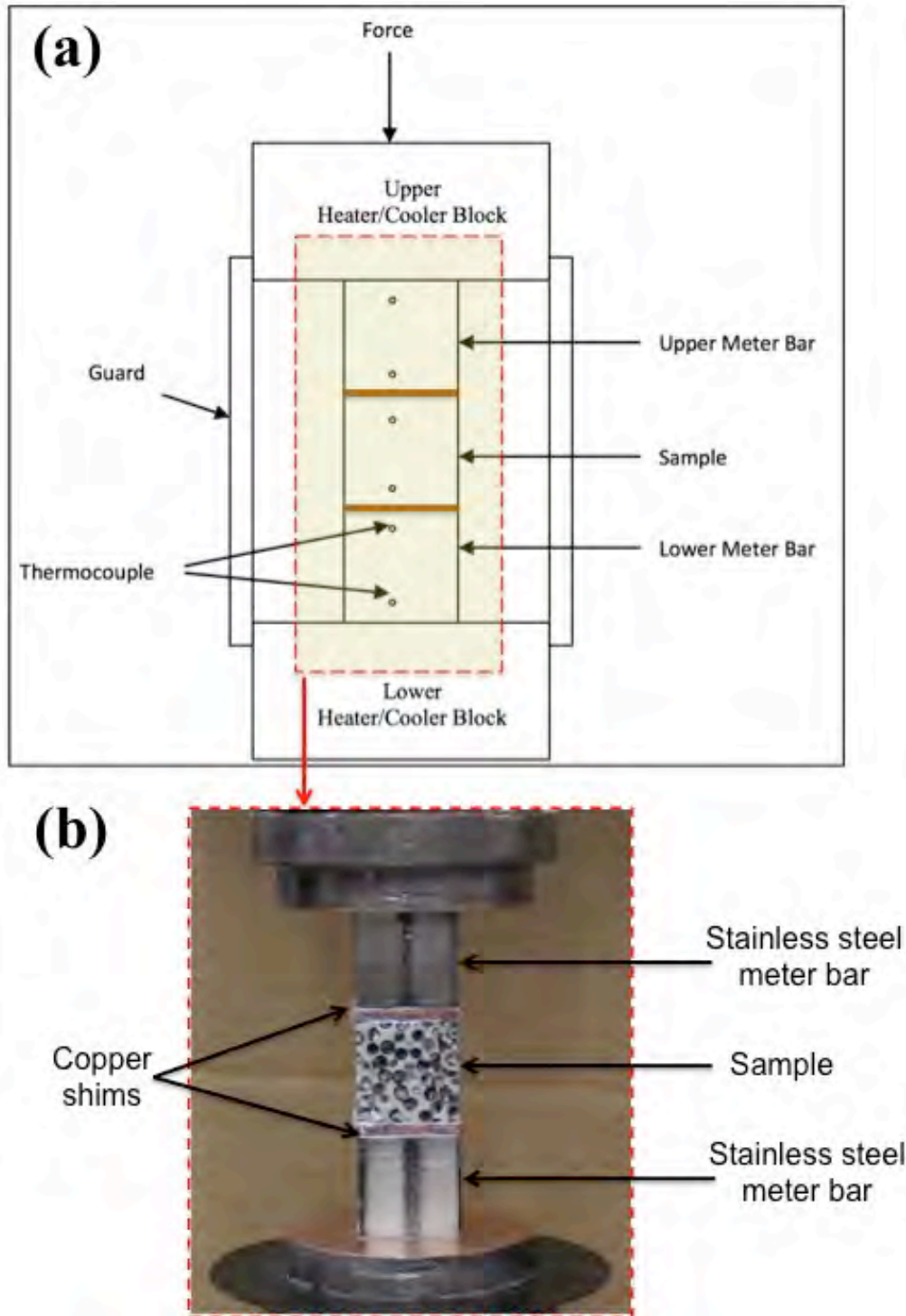
Figure 4–6: Schematic of guarded-comparative-longitudinal heat flow technique setup

During the measurement, a uniform compressive pressure of 100psi was applied on the specimen stack to ensure good contact between each interface. A temperature gradient is established using a heater on one end and a cold sink on the other end. The test apparatus was

ramped to the desired temperatures and held for sufficient time to reach steady state. The total temperature difference between the upper and lower plates was maintained at 40°C. At equilibrium conditions, the thermal conductivity is derived from the measured temperature gradients in the respective specimens and the thermal conductivity of the reference materials: two stainless steel meter bars. The tests were performed in vacuum (<200mTorr). Heat losses were minimized by use of a longitudinal insulation guard having approximately the same temperature gradient. The thermal conductivity-testing apparatus was verified with NIST SRM 1462 Stainless Steel. The data supplied with the SRM were used for the verification. With the reference material in place of the specimen, a test was run under identical conditions. Measurements on the 2mm and (4mm sphere) S-S CMFs were performed from 300°C up to 600°C at increments of 100°C, while (4mm sphere) Al-S CMF was tested from 300°C up to 500°C at increments of 100°C.

Considering the relationships for evaluating the effective thermal conductivity, the uncertainty in the measurement can be expressed as:

$$\omega_R = f\left(K, \Delta T, A, x\right) \tag{15}$$

The main uncertainty in this measurement is due to errors in determining the heat flux through the sample, which leads to a maximum error of 5% (W/m-K). The uncertainties for the thermocouples and the data acquisition readings are ±0.25^{o}C that introduces a maximum error of 0.08% between the interfaces of the sample and the stainless steel meter bars. The uncertainty associated with the load cell, thickness and cross-sectional area measurements are respectively 0.02% and 1%. The total uncertainty for the thermal conductivity measurements can be calculated using the following (root mean square) RMS method:

$$\frac{\delta\omega_R}{\omega_R} = \sqrt{\left(\frac{\delta K}{K}\right)^2 + \left(\frac{\delta\Delta T}{\Delta T}\right)^2 + \left(\frac{\delta A}{A}\right)^2 + \left(\frac{\delta x}{x}\right)^2} \tag{16}$$

For this study, the maximum uncertainty is estimated within ±5.1%.

4.5.2 Thermal Expansion Analysis

Two S-S CMF samples with respectively sphere sizes of (2mm sphere) and (4mm sphere) were chosen for coefficient of thermal expansion (CTE) measurements. The sample dimension was designed to have a length of 20mm and cross-section of 8mm by 8mm. Specimen contact

areas (top and bottom surfaces) were cut to be parallel, following by surface finishing using a progression of 240, 600, and 1200 grit papers at a wheel speed of 90rpm.

Linear thermal expansions of (2mm sphere) and (4mm sphere) S-S CMF were measured from 0°C to 400°C at 5°C/min using a commercial thermomechanical analysis equipment (TMA 202, NETZSCH-GERÄTEBAU GMBH) at Advanced Materials and Processing Branch at NASA Langley Research Center. The measurement system design was adapted from the American Society of Testing and Materials (ASTM) E831 as shown schematically in Figure 4–7. The sample was placed in a furnace enclosure, which can be maintained within a few tenths of a degree using closed-loop temperature control. The sample is positioned on a fused quartz platform and a moveable probe is placed on the top of the sample. The dimensional changes occurring as a function of time and temperature were monitored by a linear variable differential transformer (LVDT) attached to the probe. The position of the probe was set to zero on the platform. Following by raising the probe, placing the sample on the platform, lowering the probe on the sample, raising the furnace around the sample and starting the temperature program. The resulting record showed the linear thermal expansion of the CMFs samples with changing temperature. Each sample was tested twice, and the average of the two was used for calculation and comparison.
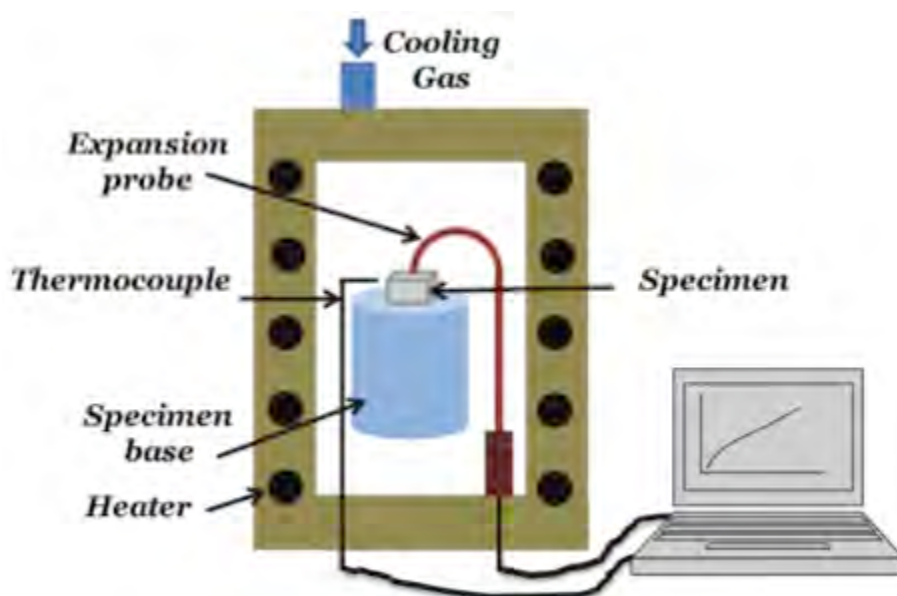
Figure 4–7: Schematic of the experimental setup of thermomechanical analyzer used for coefficient of thermal expansion measurement [14]

4.6   Flame Test

Spent fuel transportation casks are commonly used as containers for transporting radioactive waste materials from nuclear power plants to fuel reprocessing plants or disposal sites. A typical nuclear cask uses forged 304L stainless steel (SS) as an outer shielding layer (0.75" thick) to attenuate gamma rays, and beech or spruce encased in 304L stainless steel shells as impact limiter to absorb shock energy. In order to meet United States Nuclear Regulatory Commission (USNRC) standard, nuclear cask must withstand the following accident scenarios and conditions [49 CFR 173.398(d)] [15]:

- Impact test: 30-foot drop onto a flat, essentially unyielding horizontal surface

- Puncture test-a drop of 40 inches onto a six-inch diameter vertical steel bar

- **Fire test-a 30-minute fire at 800ºC**

- Immersion test-immersion in three feet of water for eight hours

CMF has been demonstrated to have excellent radiation shielding efficiency, high energy absorption capability, superior thermal performances, which make it a potential candidate for structural material in spent fuel transportation casks. In this study, (2mm sphere) S-S CMFs and control sample 304L stainless steel was fabricated to the thickness of 0.75", and then subjected to a fully engulfing fire with an average flame temperature of 800ºC for a period of 30 minutes. Figure 4–8 shows the digital image of flame test samples. Due to the size limitations of existing furnaces and high cost of full-scale nuclear cask, a small-sized horizontal propane fired burner with an opening of 6x6" and accommodating samples of 2.5x2.5x0.75" were used to carry out the flame test. The horizontal position of the samples, with the lower surface exposed to the fire, represents a fully engulfing fire with an advantage of a more homogeneous temperature distribution on the fireside of the samples. Two mineral fiber insulation boards (Figure 4–9) surrounded the sample in order to keep the other surfaces closed, mimicking an adiabatic boundary condition on the sample periphery, preventing heat and mass loss through the borders of the investigated assembly. Figure 4–10 shows the sample enclosed in fiber insulation materials. Physical properties of the samples are presented in Table 4–2.
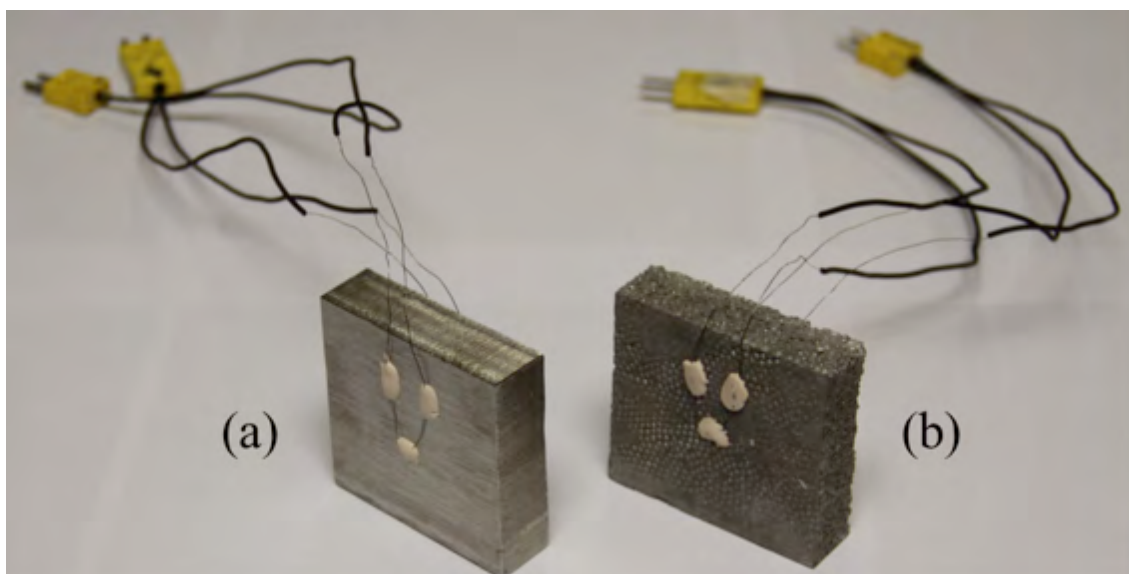
Figure 4–8: Digital images of flame test samples showing the location of thermocouples on the exposed surface: (a) 304L stainless steel, and (b) (2mm sphere) S-S CMF

Figure 4–9: Mineral fiber insulation boards surrounded the sample
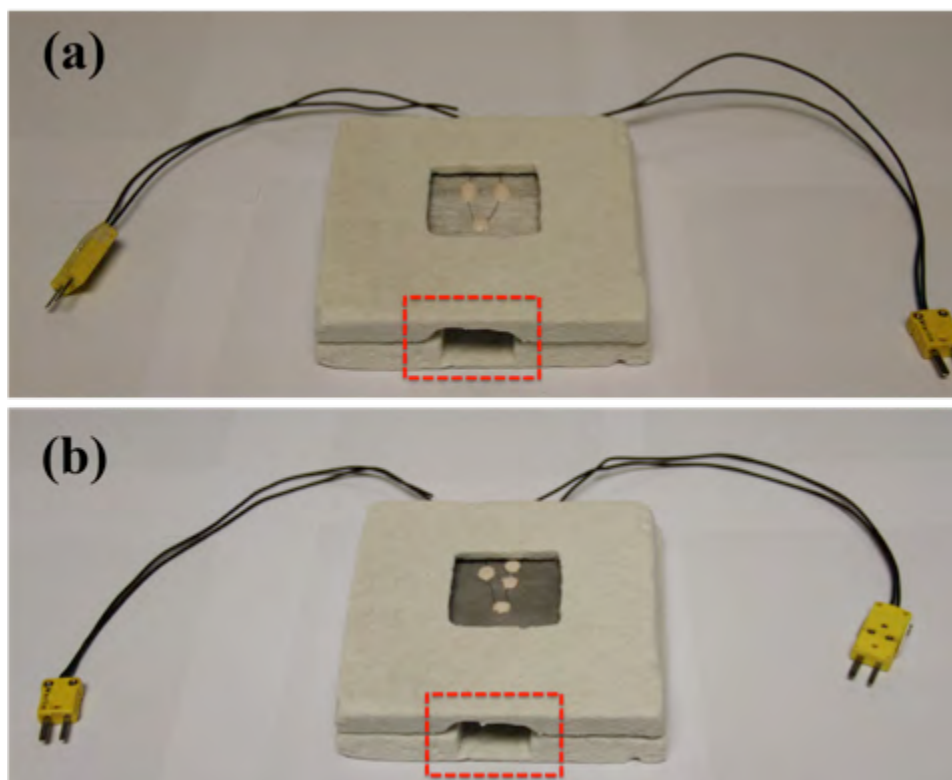
Figure 4–10: Sample enclosed in fiber insulation material: (a) 304L stainless steel and (b) (2mm sphere) S-S CMF. Dashed rectangular indicates the area for IR imaging

Table 4–2: Physical properties of (2mm sphere) S-S CMF and 304L stainless steel for flame test

Samples	Sample thickness (cm)	Sample width (cm)	Sample length (cm)	Volumetric Density (g/cm^3)
304L stainless steel	1.91	6.35	6.35	8.03
(2mm sphere) S-S CMFs	1.89	6.35	6.35	2.71

Flame test was performed at the Center for Research on Textile Protection and Comfort (T-PACC) at North Carolina State University. A schematic of the apparatus is shown in Figure 4–11, the burner with a square tray size of 50×50cm was operated with propane based typical low-calorific value fuels. The installation of the burner was performed in accordance with ASTM F2700 guidelines. The sample was supported on an adjustable ring clamp fastened on the pole of a metal support stand. The height of the ring clamp was adjusted to be 18cm above the burner so that an average flame temperature of 800°C touched the center bottom of the sample. Temperature measurement was performed by Type-K (chromel alumel) probe-style

thermocouples, which was connected to a computer and LabVIEW interface via a data acquisition control unit (Agilent 34970A). Three thermocouples were provided, one for measuring the temperature of the flame reaching the bottom of the sample, the other two for determining the temperature from the upper and lower surfaces of the sample. The probes of the thermocouples are held horizontally with the tip reaching the centerline. The junctions were fixed in intimate contact with the specimen by means of high temperature cement (Omegabond 600") that was cured at room temperature 24 hours before commencing the measurements. An infrared thermo-camera (FLIR A325sc), featuring 320 by 240 pixels, with detector pitch of 25um, and recording 30 frames per second, was implemented to further explore the sample and flame temperature. The camera was positioned on a tripod with the imaging field of view just above the supporting ring, capturing one of the side surfaces of the sample. The camera lens was placed 25cm from the centerline of the sample to perform accurate quantitative temperature measurements.
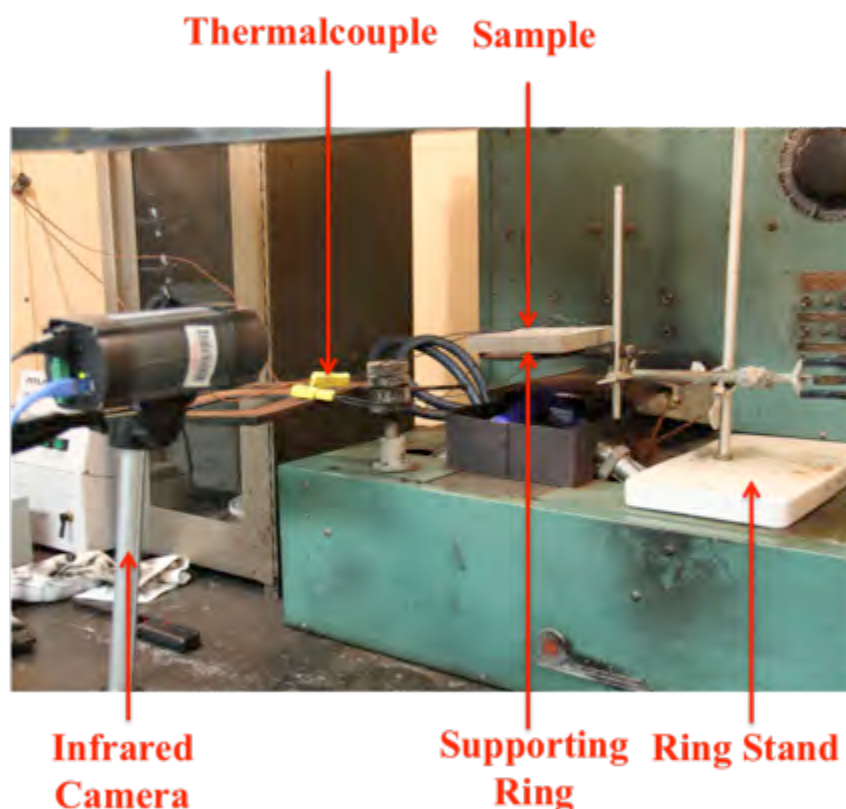
Figure 4–11: A schematic of the flame test setup

CHAPTER 5   RESULTS AND DISCUSSIONS

5.1   X-ray Attenuation of CMFs
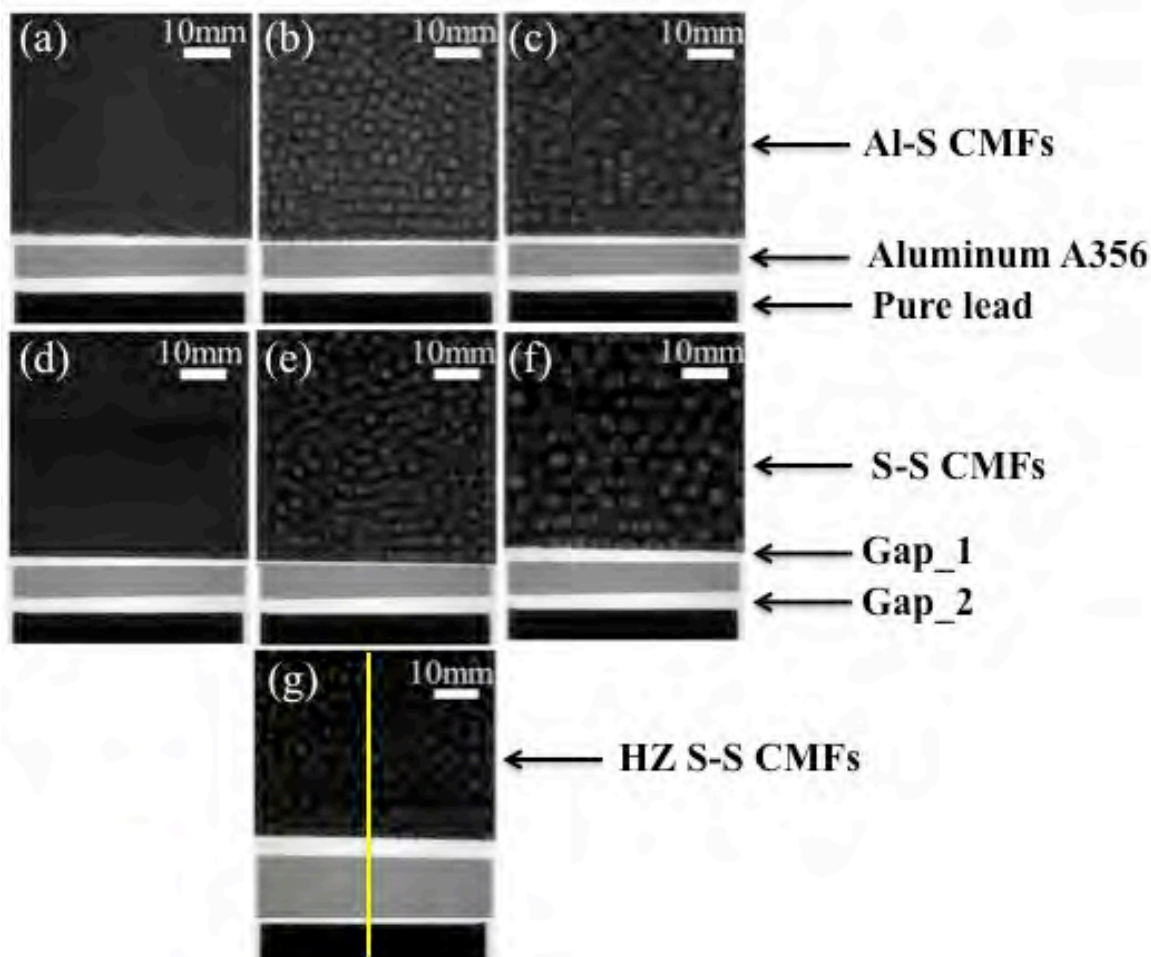
Figure 5–1: Micro-CT 2D projection images of (a) (2mm sphere) Al-S CMF, (b) (4mm sphere) Al-S CMF, (c) (5.2mm sphere) Al-S CMF, (d) (2mm sphere) S-S CMF, (e) (4mm sphere) S-S CMF, and (f) (5.2mm sphere) S-S CMF, and (g) (4mm sphere) HZ S-S CMF, in each projection image (From top to bottom), the materials are respectively CMF, Aluminum A356, and pure lead

Figure 5–1 shows projection X-Ray images of close-cell CMFs in comparison with two reference materials (aluminum A356 and pure lead which are shown at the bottom of each figure). As can be seen, the porous media within the matrix is uniform, homogeneous and isotropic, which provide close-cell CMFs excellent consistency and stability in engineering design applications. In addition, these images open up an opportunity to directly visualize

complex 3D pore structures into simplified 2D description and allow for more detailed correlations to be calculated. Regardless of sphere size, steel-steel CMFs (darker in the image) seems to be more absorbing comparing to Al-steel CMFs, and both steel-steel CMFs and Al-steel CMFs offer more X-ray shielding efficiency than that of Aluminum A356, and less attenuation than that of lead. This result may be attributable to photoelectric absorption (τ), which is a dominant photon interaction mechanism at relative low energy radiation [16]. This mechanism is strongly influenced by Z_{eff} of the absorber material with higher Z_{eff} of the material having greater probability of photoelectric interaction to occur, and the probability is given approximately by the relation $\tau \propto Z_{eff}^5 / E^{7/2}$ [17]. In our previous study, the values of Z_{eff} for steel-steel CMF, Al-steel CMF, Aluminum A356 and lead are calculated to be 26.8, 21.4, 11.7 [18] and 82, respectively. Therefore, X-ray shielding efficiency of the samples increases significantly with increasing of Z_{eff}. The porosities in 2mm, 4mm, and 5.2mm steel-steel CMFs were measured respectively to be 43%, 41%, and 44%, therefore, X-ray shielding capability of steel-steel CMFs are relatively independent of sphere sizes. Whereas in Al-steel CMFs, the porosities were dropped to 39%, 38%, and 40% due to lower porosities in Aluminum cast matrix in Al-S CMF compared to steel matrix in S-S CMF processed by powder metallurgy sintering. Lack of complete penetration of molten Al between spheres during casting can leave some voids in the matrix of Al-Steel CMF. Similarly, the shielding efficiency of Al-steel CMFs is unaffected by changing of sphere sizes.

Figure 5–2 presents the corresponding vertical line profile from top to the bottom in each projection image in Figure 5.1. Grey value indicates the total number of pixels corresponding to the transmitted intensity level. High peaks with more grey values indicate more photon transmission, whereas low peaks show less photon transmission. It can be clearly seen that close-cell CMFs are more effective in X-ray shielding as compared to Aluminum A356 at the same areal density. Lead exhibits better shielding capability than that of close-cell CMFs. The gaps in between CMF and Aluminum A356, as well as A356 and lead were included in each profile plot, which were shown as two narrow sharp peaks at the distance of 50cm and 60cm. The profile line in the range 0-50 cm indicates porous structure in CMFs samples. The profile line in the range 0-50cm indicate porous structure in CMFs samples, (5.2mm sphere) CMFs are more wavy compared to (2mm sphere) CMFs, resulted from the relatively lager hollow sphere size.
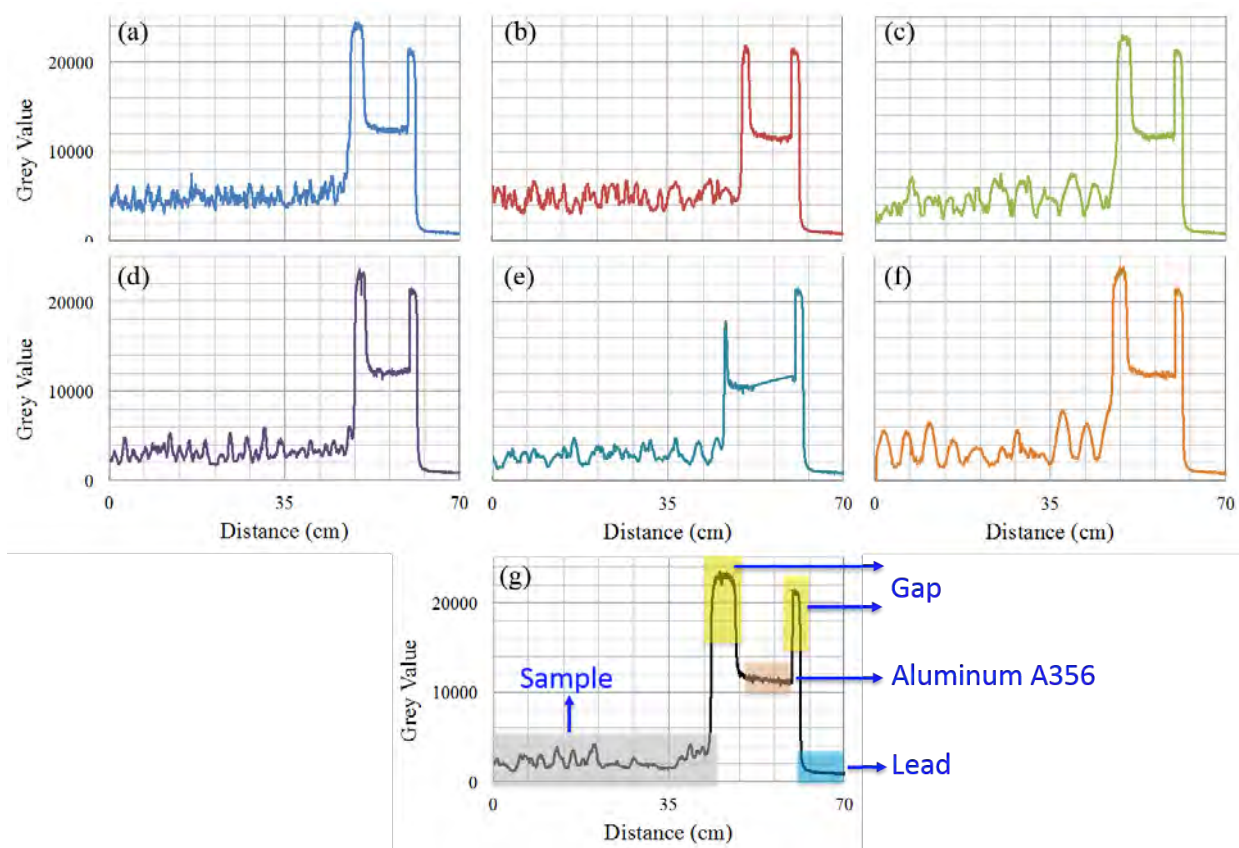
Figure 5–2: Vertical line profile showing the mean gray value along each projection image from top to bottom in Figure 5–1: (a) (2mm sphere) Al-S CMF, (b) (4mm sphere) Al-S CMF, (c) (5.2mm sphere) Al-S CMF, (d) (2mm sphere) S-S CMF, (e) (4mm sphere) S-S CMF, and (f) (5.2mm sphere) S-S CMF, and (g) (4mm sphere) HZ S-S CMF, in each projection image (From top to bottom), the materials are respectively CMF, Aluminum A356, and pure lead

In order to quantitatively measure shielding effectiveness of samples, the mean pixel count was calculated by using Image J program and normalized with sample density (shown in Figure 5–3).

Figure 5–3 shows mean grey value per unit density of all samples. As can be seen, for a given areal density of shielding material ($2g/cm^2$), the effect of sphere sizes on the shielding effectiveness of both Al-S and S-S CMFs is insignificant. This can be due to the fact that the sphere wall thickness (t) to sphere radius (r) ratio is the same in all samples and as such, the amount of shielding material in all samples is the same, regardless of their sphere sizes.

However, the smaller spheres seem to be more efficient in general due to the fine fluctuation in the gray value profile of their 2D Micro-CT images. It was calculated that Al-S CMFs and S-S CMFs are respectively 145% and 275% more effective in shielding X-rays compared to Aluminum A356. This is attributed to higher contents of iron in the sphere wall and within S-S CMFs matrix. This shielding efficiency can be further enhanced to 398% in HZ S-S CMFs as a result of additional elements of tungsten (12.5 wt%) and vanadium (5.0 wt%) in the T15 matrix. Even though pure lead is still the predominant shield material for X-ray, its toxic nature to human organ and tissues has largely limited its applications. It is worth noting that, in Figure 5-3, HZ S-S CMFs have an average density of 2.69 g/cm^3, and it is found to be 25% more absorbing X-rays compared to regular S-S CMFs (with an average density of 2.73 g/cm^3). This encouraging result is a breakthrough in shielding X-rays and opens the door for future work on further improving the shielding capability of CMFs while maintaining the advantages of its unique low-weight and outstanding physical and mechanical characteristics.
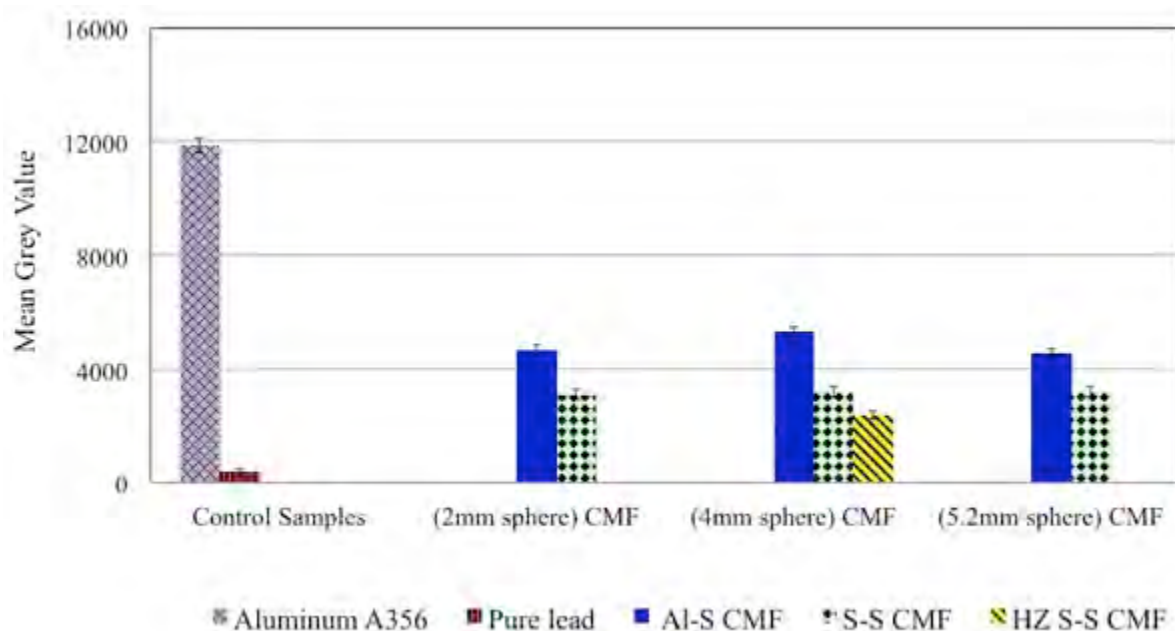
Figure 5–3: Histogram showing X-ray shielding efficiency of CMFs, Aluminum A356 and lead

5.2 Gamma Attenuation of CMFs and open cell aluminum foam with filler

Transmission gamma ray for all samples at six different photon energies are shown in Figure 5–4. In each plot, the transmission profile decreases with increasing of sample thickness, which can be explained using: $I = I_0 \exp(-ux)$, where u (cm^{-1}) is the linear attenuation coefficient and x (cm) is the sample thickness.

At higher energy level (1.332MeV, 1.173MeV and 0.662MeV), the transmission curves are overlapping. This is due to the fact that the effective interaction mechanism between gamma ray and matter in energy ranges from 0.5MeV to 10MeV is Compton scattering. Compton scattering involves the scattering of photons by charged particles where both energy and momentum are transferred to the charged particle, while the photon moves off with a reduced energy and a change of momentum [22]. In this interaction, Compton scattering causes increasing function of electron density of the material. Hence, all samples display similar trend under sources ^{60}Co and ^{137}Cs. Regardless of the type of samples, approximately 10%, 20%, and 45% of incident photon with energies of 1.332 and 1.173MeV were attenuated at areal densities of 2, 5 and 10g/cm^2, respectively. An increased attenuation of 15%, 30%, and 55% can be observed at a lower energy of 0.662MeV with areal densities of 2, 5 and 10g/cm^2, respectively.

When energy drops to 0.356MeV, photoelectric absorption (α) starts to take place. The difference between Al-S CMFs and S-S CMFs in shielding gamma rays in such energy levels is distinguishable in Figure 5–4, Figure 5–5, Figure 5–6. The photoelectric absorption process converts electromagnetic energy of a gamma ray photon into kinetic energy of a charged particle [24]. At a given photon energy, the interaction is proportional to the effective atomic number (Z_{eff}) by the relation $\left(\alpha \propto Z_{eff}^5 / E^{7/2}\right)$ [17]. As can be seen in Figure 5-4 a clear difference between Al-S CMF, S-S CMF and Aluminum A356 for attenuating gamma rays can be observed. This is mainly due to the fact that higher effective atomic number Z_{eff} can offer better attenuation efficiency. As given in **Table 5- 1**, the average values of Z_{eff} (0.08MeV) for HZ S-S CMF, S-S CMF, Al-S CMF and Aluminum A356 are calculated to be 29.5, 26.5, 22.4, and 13.3, respectively. With further decreasing of the photon energy to 0.060MeV, the incident gamma ray

flux was fully shielded by CMFs at areal density of 5g/cm^2. The specimens with greater Z_{eff} (**Table 5- 1**) show better attenuation efficiency.

Table 5- 1: Effective atomic number of CMFs and Aluminum A356

	Zeff (0.081 MeV)	Zeff (0.060 MeV)
(2mm sphere) S-S CMF	26.5	26.8
(2mm sphere) Al-S CMF	22.5	20.9
(4mm sphere) S-S CMF	26.5	26.8
(4mm sphere) HZ S-S CMF	**29.5**	**38.0**
(4mm sphere) Al-S CMF	22.4	21.4
(5.2mm sphere) S-S CMF	26.5	26.7
(5.2mm sphere) Al-S CMF	22.4	20.9
Aluminum A356	13.3	11.7

The values of Z_{eff} for steel-steel CMF, Al-steel CMF and Aluminum A356 are calculated to be 26.8, 21.4, and 11.7, respectively. As shown in Figure 5–5, the attenuation of incident gamma radiation is determined mainly by photoelectric absorption and is indicated by tabulated XCOM data that photoelectric absorption for steel-steel CMF, Al-steel CMF and Aluminum A356 contributes, respectively, 88.44%, 79.49% and 41.9% of the total attenuation. This severe dependence of the photoelectric absorption probability on Z_{eff} is a primary reason for the preponderance of close-cell CMFs in ^{241}Am shields.
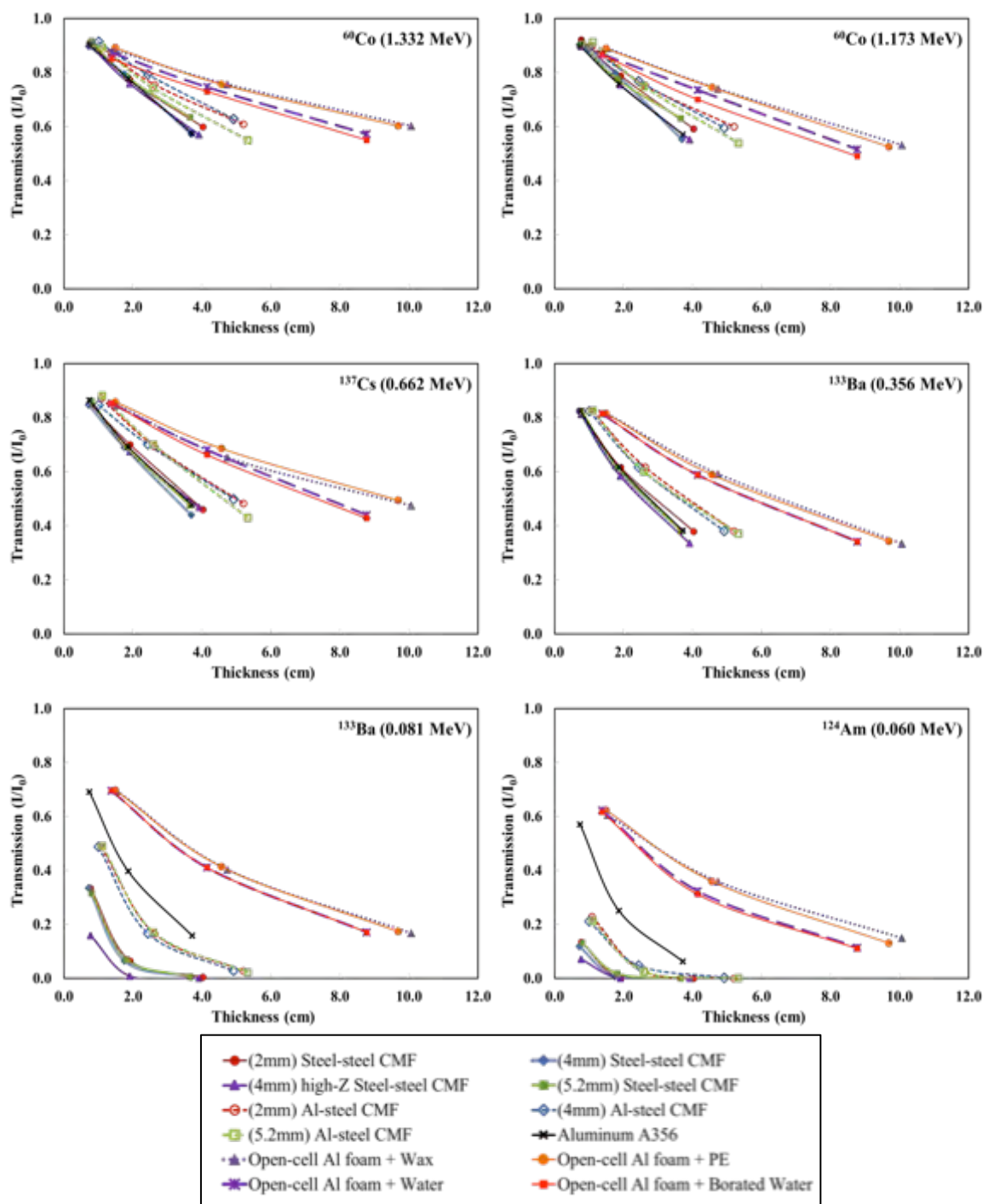
Figure 5–4: Gamma transmission as a function of thickness for all specimens at six different photon energies (a) ^{60}Co (1.332MeV), (b) ^{60}Co (1.173MeV), (c) ^{137}Cs (0.662MeV), (d) ^{133}Ba (0.356MeV), (e) ^{133}Ba (0.081MeV), and (f) ^{241}Am (0.060MeV)
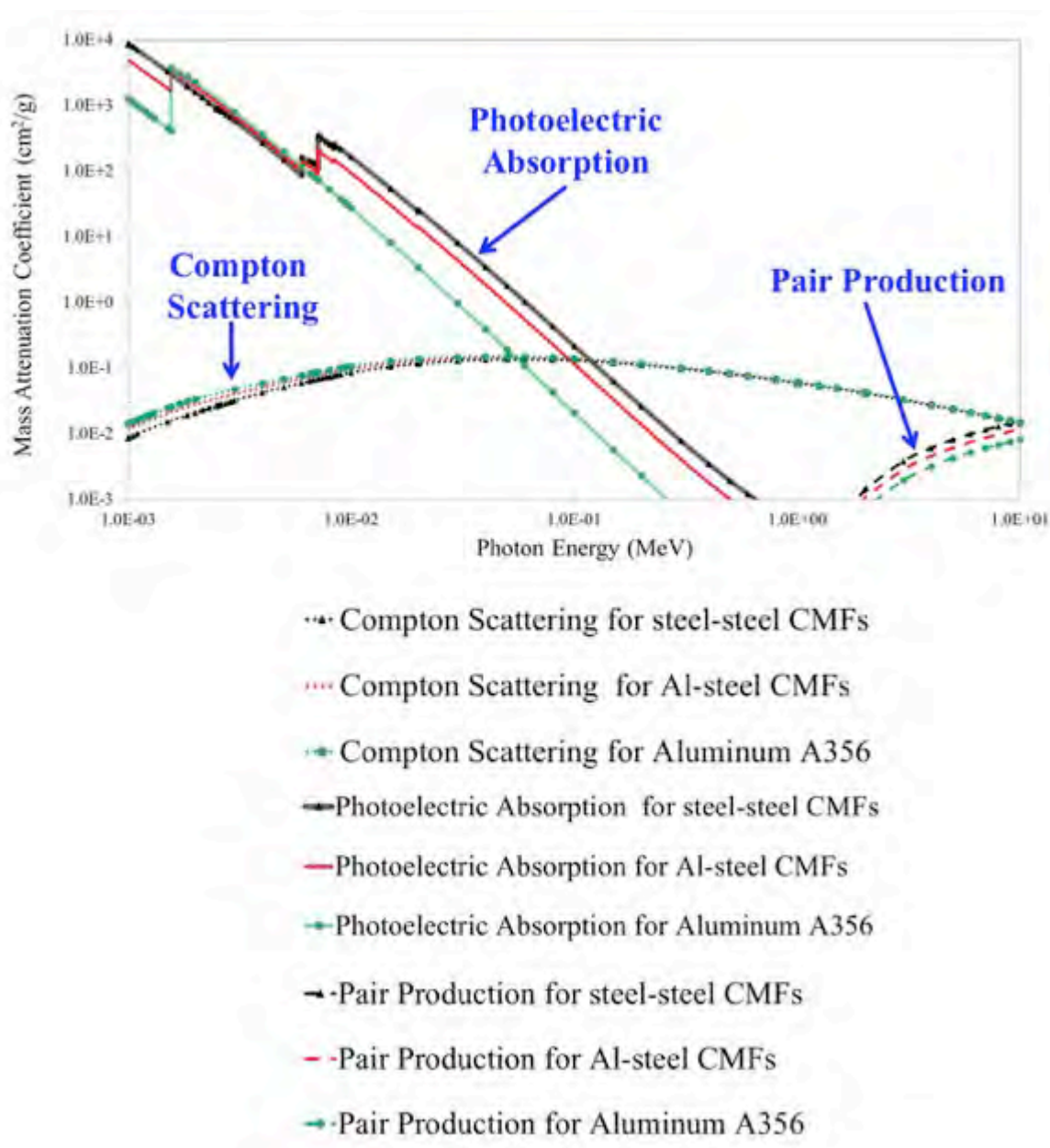
Figure 5–5: Three different photon interaction mechanisms with steel-steel CMF, Al-steel CMF, and Aluminum A356 from XCOM results

Figure 5–6 shows transmission as a function of photon energies through all six sets of samples at each areal density, the displayed curves can be divided into two regions: I and II, with region I covers source energies smaller than 0.662MeV whereas region II covers source energies larger than 0.662MeV. In region I, transmission increases significantly with increasing photon energy, as given in Figure 5–6a, steel-steel CMF and Al-steel CMF shielded, respectively, 80%

and 90% of the incident photon with energy of 0.060MeV, whereas Aluminum A356 and open-cell Al foam with fillers shielded 40% of the incident photon. Steel-steel CMF was found to be 105% more effective than Aluminum A356 even at similar density, and Al-steel CMF exhibits 84% more effective in photon shielding with 28% less density compared to Aluminum A356. Comparing Figure 5–6b and Figure 5–6c, it is clear that attenuation increases as areal density increases; that incident photon was 100% shielded by steel-steel CMF and Al-steel CMF at areal density of only 5g/cm^2 whereas open-cell Al foam with fillers shielded approximately 70% and Aluminum A356 shield 75% at the same areal density. With further increasing the areal density to 10g/cm^2, there were still 10% of incident photon energies passing through the open-cell Al foam with filler samples. The better performance of close-cell CMFs in low energy radiation attenuation is resulting from photoelectric absorption, which has a strong dependence on Z_{eff} of the attenuator. In region II, transmission increases slowly with increasing photon energy, and displaying curves were closely overlapping. This can be attributed to Compton scattering (σ) which is the predominant interaction mechanism for medium energy range (0.5MeV to 10MeV), σ is relatively independent of both incident photon energy and Z_{eff}, but it is strongly proportional to the electron density in the absorber, all elements contain approximately the same number of electrons per unit mass with the exception of the heaviest elements and hydrogen, hence, all samples exhibit close attenuation in region II. It can therefore be inferred that close-cell CMFs are ideal for shielding at lower energy level. Therefore, in applications where more physically rigid, compact shielding is required, such as shielding of radiation sources for medical diagnostic devices, industrial gauges, and cargo inspection portal, steel-steel CMF may be preferred to benefit operating performance, economics, safety, and reliability of the system. In other applications, where light-weight is required, such as components of radionuclide carriers and lower level nuclear waste canister, Al-steel CMF may be preferred with additional energy absorption and heat rejection capabilities. Open-cell Al foam with fillers is less effective in gamma attenuation, but can be preferred as neutron absorbers when filled with high hydrogen content materials, which will be discussed in the next section (section 5.3).
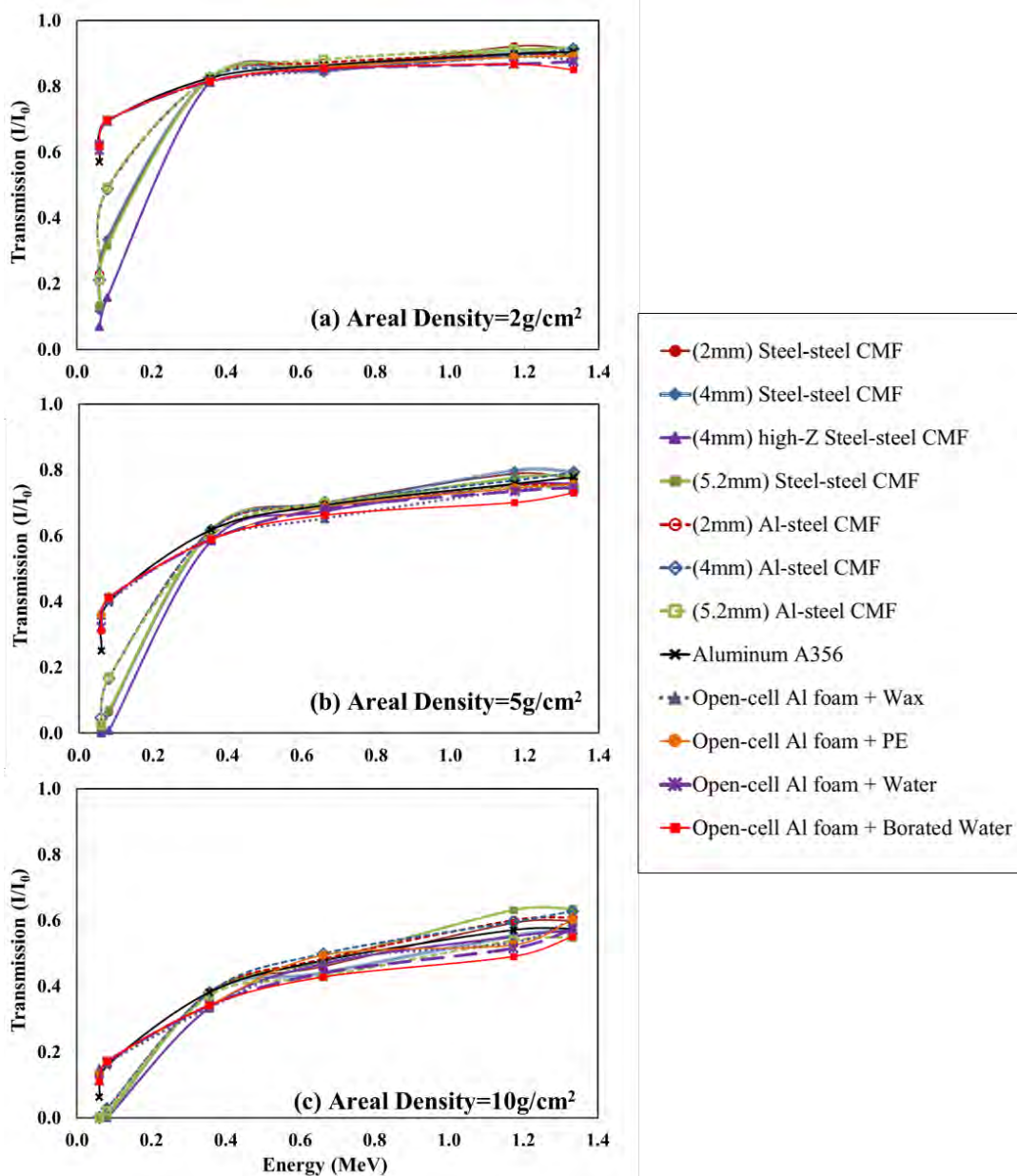
Figure 5–6: Gamma transmission as a function of energy for all specimens at different areal densities (a) areal density=2 g/cm^2, (b) areal density=5 g/cm^2, and (c) areal density=10 g/cm^2

5.3   Neutron attenuation of CMFs and open cell aluminum foams with filler

5.3.1   Effect of sample thickness on neutron shielding

Figure 5–7 shows neutron transmission as a function of thickness in all eleven sets of samples. It can be clearly seen that the transmission decreases with increasing of sample thickness. Regardless of the type of samples in close-cell CMFs, approximately 20%, 40%, and 70% of the incident neutrons were attenuated at areal densities of 2, 5 and 10g/cm², respectively. In Figure 5–7b, open-cell Al foam with fillers shielded up to 96% of the incident neutron flux at an areal density of 2g/cm². With further increasing of the sample thickness, neutrons were 100% attenuated. The equation that can explain the strong dependency of neutron transmission on the sample thickness is: $T = \exp(-\Sigma x)$ in which transmission is decreasing exponentially with increasing of the sample thickness.

5.3.2   Effect of type of samples on neutron shielding

As summarized in Table 3–4 and Table 3–, open-cell Al foam infiltrated with wax, PE, water, or borated water contain respectively 14.8%, 11.6%, 11.2%, and 11.1% (wt) of hydrogen. The presence of low Z element, hydrogen, serves as excellent neutron absorbers to capture thermal neutrons and endows open-cell Al foams with fillers with superior neutron attenuation performance compared to closed cell CMFs. In open-cell Al foam with fillers, scattering is the predominant interaction mechanism, while in close-cell CMFs the dominating mechanism is "radiative capture". This is due to the fact that close-cell CMFs contain large amount of high-Z elements: Mn, Mo and Fe, which are very effective for such neutron absorption. As mentioned before, embedding the steel hollow spheres in stainless steel or Al matrix, respectively, produced steel-steel CMF and Al-steel CMF. Regardless of sphere size, as shown in Figure 5–7a, steel-steel CMFs perform better in terms of neutron attenuation than that of Al-steel CMFs. This is due to the presence of higher content of high-Z element such as Fe in steel-steel CMF matrix. Neutron absorption cross-section of Fe (2.59b) used in steel-steel CMFs matrix ranges over ten times that of Al (0.213b) in Al-steel CMFs matrix. As a result, neutrons were absorbed more efficiently in steel-steel CMFs than that of Al-steel CMFs.
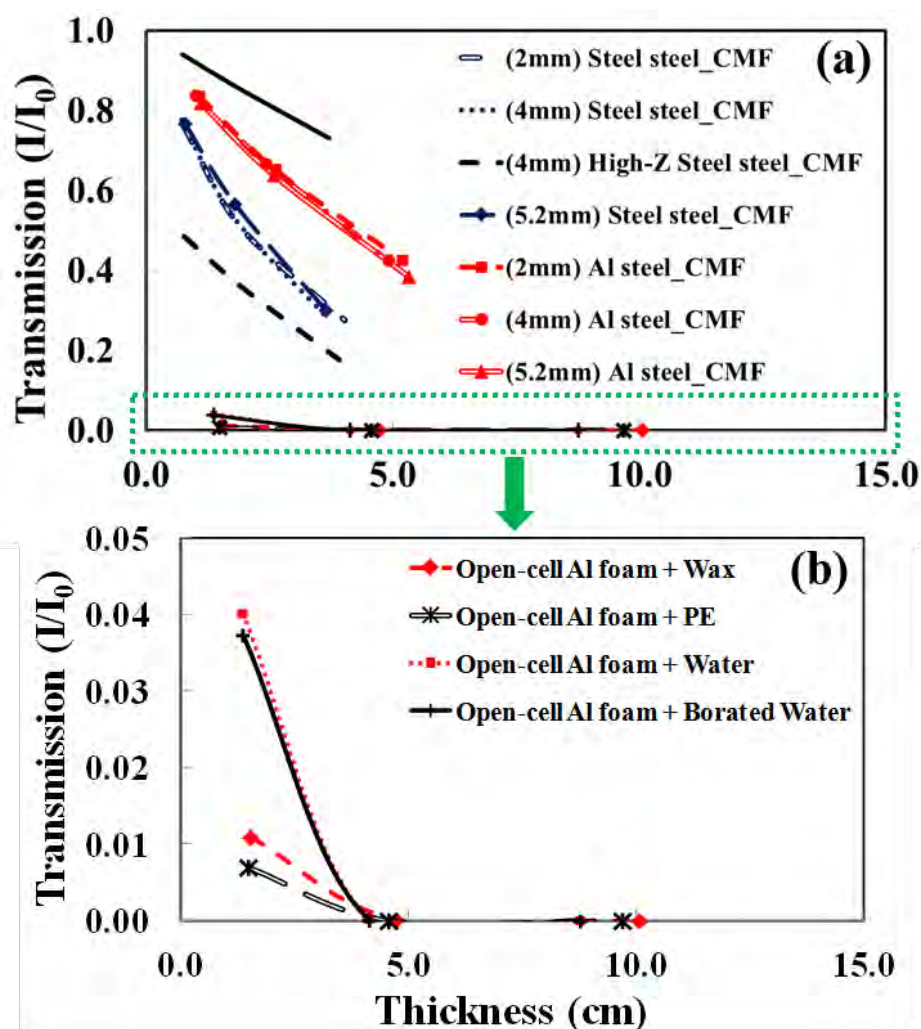
Figure 5–7: Neutron transmission as a function of sample thickness for (a) all samples, and (b) open-cell Al foam with fillers

As shown in Figure 5-7, it is obvious that HZ matrix enhances the neutron attenuation of the foams considerably. The (4mm sphere) HZ S-S CMF was found to be respectively, 60%, 100%, and 180% more effective than those of S-S CMF, Al-S CMF, and Aluminum A356. It is well known that a large neutron cross-section is the key criterion for better neutron attenuation capability. The significant improvement of HZ S-S CMF in terms of neutron shielding is attributed to the presence of high-Z elements such as tungsten and vanadium in the matrix materials. The neutron cross-section of tungsten and vanadium are respectively 18.4b and 5.06b. It should be noted that tungsten and vanadium are identified as low activation elements [24], which can offer an additional advantage of radiation damage resistance to HZ S-S CMF. Moreover, it is anticipated that the presence of pre-existing air trapped inside the spheres as well

as micro-porosity inside sphere walls and the matrix could reduce volumetric swelling in case of exposure to high-flux neutron. These unique properties maximized the attractiveness of CMFs in general and new class of HZ S-S CMF in particular for nuclear structural applications from the viewpoints of safety and stability

It is worth noting that both close-cell CMFs and open-cell Al foam with fillers perform better on neutron attenuation than that of Aluminum A356 with additional advantage of lightweight, good mechanical energy absorption and better thermal isolation, which are key technological requirements for the development of practical radiation shields.
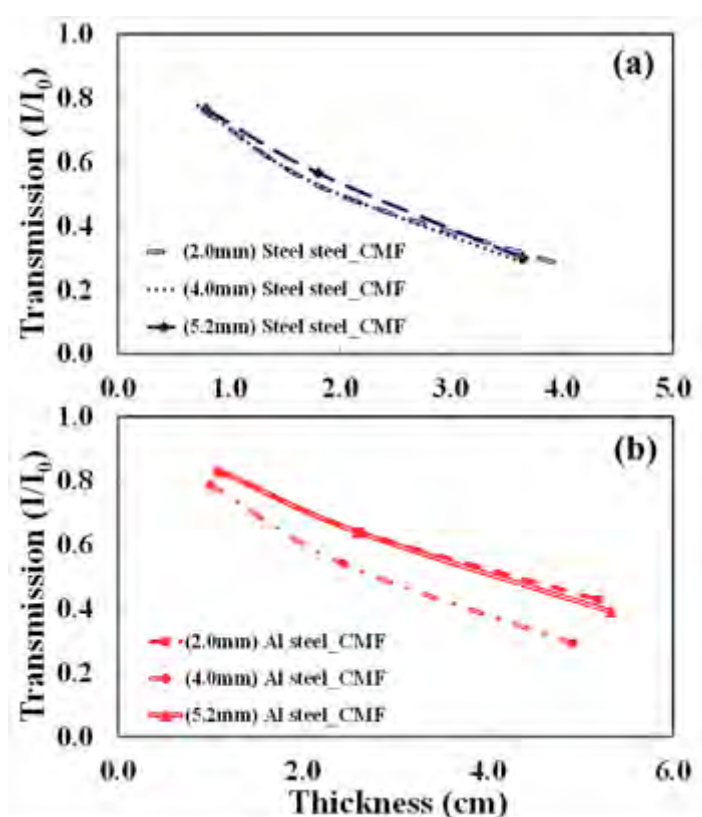
Figure 5–8: Neutron transmission as a function of sample thickness for (a) steel-steel CMFs, and (b) Al-steel CMFs

Effect of sphere size on neutron attenuation of steel-steel CMFs: The neutron transmission of steel-steel CMFs with different sphere sizes as a function of sample thickness is represented in Figure 5–8a. It was found that the transmission curves are closely overlapping with each other for all samples with different sphere sizes. This is due to the fact that the ratio of sphere wall thickness (t) to the radius of sphere (R) is maintained constant for all sphere sizes. As

a result, the total amount of air inside the spheres is balanced out by total amount of sphere wall and matrix material in all samples despite of their different sphere sizes. As given in Table 5–1: Comparison of variety of spheres used in close-cell CMFs, all spheres with diameters of 2.0, 4.0 and 5.2mm possess a similar t/R ratio. At the same time, since the matrix and spheres are from similar material, the difference in the contact area of spheres and matrix in samples with different sphere sizes are not having any major effect on their shielding behavior. Therefore, attenuation efficiency of all steel-steel CMFs is relatively independent of sphere size.

Table 5–1: Comparison of variety of spheres used in close-cell CMFs

Sphere size (mm)	Sphere wall thickness t (mm)	Sphere outer radius R (mm)	t/R
2.0	0.104	1.02	0.1023
4.0	0.196	1.76	0.1111
5.2	0.244	2.59	0.0943

Table 5–2: Physical parameters of steel-steel CMFs

Steel-steel CMFs	Sphere wall porosity (%)	Sphere wall density (g/cm3)	Matrix porosity (%)	Matrix density (g/cm3)
2.0mm	8	7.36	32.61	5.39
4.0mm	6	7.52	0.33	7.97
5.2mm	4	7.68	42.24	4.62

Effect of microstructure on neutron attenuation of steel-steel CMFs: SEM observation was carried out to investigate the effect of microstructure on neutron attenuation of various CMFs. Figure 5–9(a-c) give SEM images of steel-steel CMF samples produced with 2.0, 4.0, and 5.2mm spheres. It can be seen that sphere walls and matrix are bonded well and no precipitation is presented. As indicated in Fig 5-9, all spaces between spheres were completely filled with steel powder; the steel matrix is in close contact and well bonded to sphere walls. There are some micro-porosities in the microstructure of the material, which has minimal effect on neutron shielding performance of CMFs which seems to be negligible.
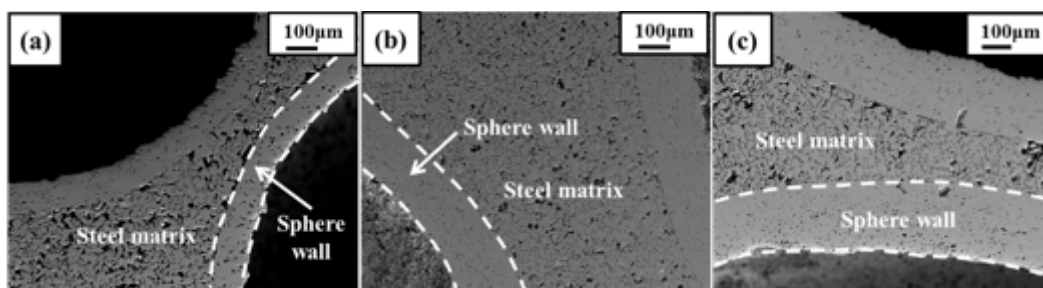
Figure 5–9: SEM images of (a) 2.0mm, (b) 4.0mm and (c) 5.2mm steel-steel CMFs showing minor porosity differences in the matrix and sphere wall, dashed line showing the wall thickness

The porosities in matrix and within sphere wall for each sample were evaluated using imaging J 47 [19]. The densities were then calculated by using equation (1), in which ρ_s of both sphere wall and the matrix was considered to be 8.0 g/cm^3. Details are listed in Table 5–2. These results will be used later in modeling the shielding behavior of steel-steel CMFs against neutrons.

Effect of sphere size on neutron attenuation of Aluminum-Steel CMFs: The transmission of Al-steel CMFs with different sphere sizes as a function of thickness is represented in Figure 5–8b. It can be seen that 4.0mm Al-steel CMF clearly dominates 2mm and 5.2mm Al-steel CMFs in terms of neutron attenuation while the transmission curves of 2.0mm and 5.2mm Al-steel CMFs are closely overlapping. This may be attributable to three possible factors: spheres removal from sample surfaces, voids between spheres and intermetallic phases within Al matrix. The first factor is only a surface effect, while the last two factors have volumetric effect.

During the process of casting Al-steel CMFs, molten Al rose up to the top of the mold and filled the interstitial space between the spheres. By decreasing the sphere size, unfilled porosities and voids will increase due to the viscosity of the molten Al. Figure 5–10 shows the voids between spheres owing to lack of aluminum penetration. While the argue sounds acceptable, one may raise the question about better performance of 4 mm sphere CMF compared to that of 5.2 mm sphere CMFs. This small deviation can be attributed to the smaller t/r ratio (Table 5–1) in 5.2 mm spheres compared to that of 4 mm spheres, which translates in to a smaller amount of sphere wall material in front of the neutron beam in the 5.2 mm sphere CMF samples. As such, even though there are less voids in between 5.2 mm spheres, the slightly

higher t/r ratio in 4 mm spheres, caused their better performance compared to 5.2 mm sphere CMfs.
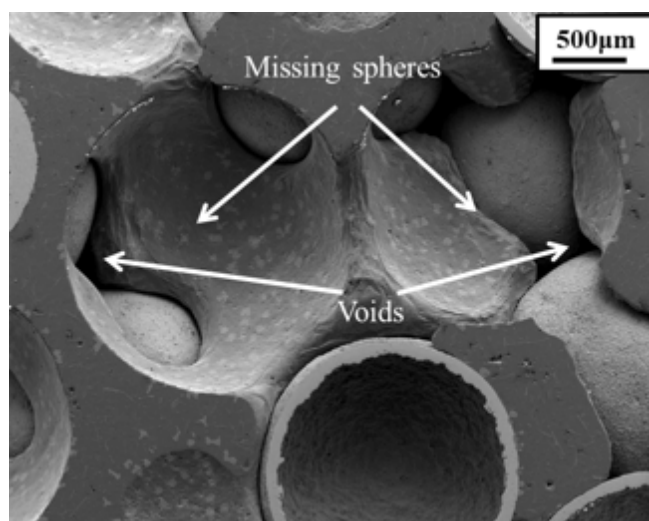
Figure 5–10: SEM images of 2.0mm Al-steel CMFs showing missing spheres and voids in Al matrix

Spheres removal was mainly caused during sample preparation process, such as cutting and ultrasonic cleaning. As indicated in Figure 3–2 and Figure 5–10, the missing spheres in Al-steel CMFs are due to the presence of brittle intermetallics in between the spheres and the matrix as well as lack of complete penetration of viscous molten Al into the empty spaces between spheres. Since spheres removal is a surface effect, it was speculated that its influence on shielding efficiency would be more severe in lower areal density samples such as those with areal density of 2. Further microstructural investigation has become necessary to better understand the differences between the neutron attenuation of Aluminum-steel CMFs.

Effect of microstructure on neutron attenuation of Aluminum-Steel CMFs: The use of dissimilar materials for spheres and matrix in Aluminum-Steel CMFs resulted in the formation of intermetallic phases during solidification process.

Shown in Figure 5–11 (a-c) are SEM images of Al-steel CMFs produced with 2.0, 4.0, and 5.2mm steel spheres. Figure 5–11 (d-f) are zoomed in SEM images taken from marked area (dash line) of Figure 5–11 (a-c) at higher magnification with sphere wall-matrix intermetallic layer highlighted. It can be seen from 4.0mm Al-steel CMFs samples, Figure 5–11b and Figure 5–11e, that three major kinds of precipitates were formed due to interdiffusion of elements between spheres and matrix: interface layer around sphere wall, plate shape and needle shape

precipitation distributed within the matrix. The intermetallic layer has been observed to be more predominant in 4.0mm Al-steel CMFs (110.89μm ±10.20μm thick) than in 5.2mm samples (10.01μm ±0.20μm thick). In the SEM images of 5.2mm Al-steel CMFs sample (Figure 5–11c) and Figure 5–11f, the lower contact area between spheres and matrix resulted in less diffusion flux between the two, which greatly decreased the formation of intermetallic layers around sphere wall as well as plate shape and needle shape precipitations in the matrix. Owing to the lower percentage of intermetallic phases, 5.2mm Al-steel CMFs is less efficient in attenuating neutrons as compared to 4.0mm Al-steel CMFs. 2.0mm Al-steel samples were expected to exhibit a better neutron attenuation behavior due to their higher sphere-matrix interfacial areas.
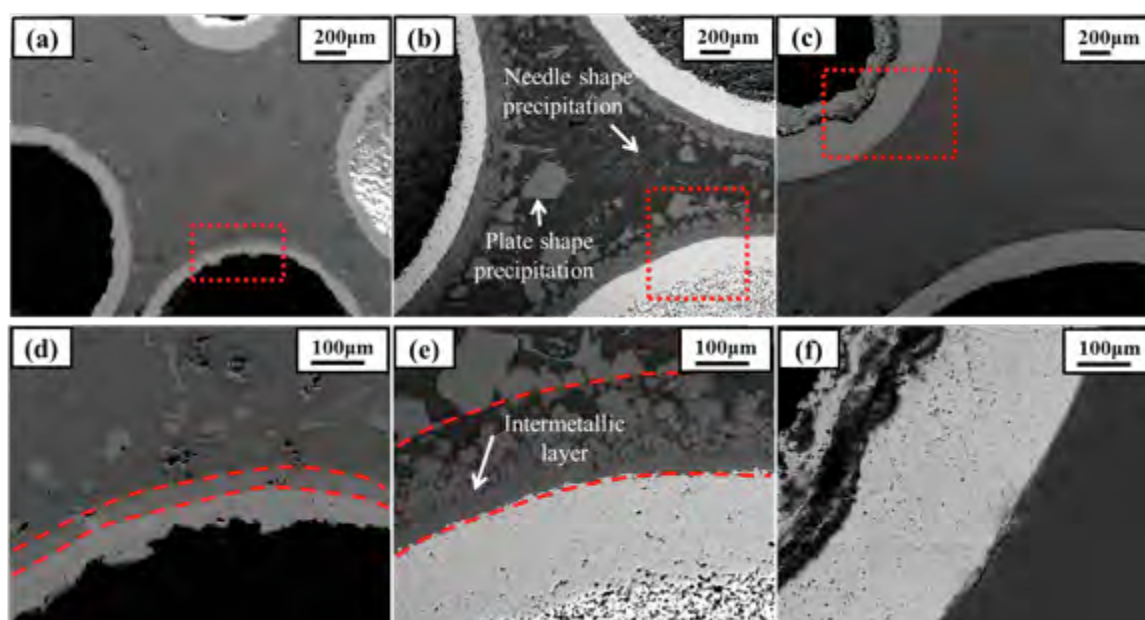
Figure 5–11: SEM images of (a) 2.0mm, (b) 4.0mm, and (c) 5.2mm Al-steel CMFs showing plate shape and needle shape precipitations, dashed line showing intermetallic layer. (d), (e), and (f) are respectively enlarged images from boxed area of (a), (b), and (c)

However, higher percentage of voids in 2.0mm Al-steel CMFs lowered the contact area between spheres and matrix causing the formation of a thinner intermetallic layer at their interface and lower percentage of plate shape and needle shape precipitation in the matrix (Figure 5–11a and Figure 5–11d). All of the above may have resulted in the decrease in the shielding efficiency of 2.0mm Al-Steel CMFs.

Chemical compositions of all intermetallic phases and their corresponding densities were calculated through equation (2) are given in Table 5–3. Image J was utilized to evaluate the

dimensions of features in the microstructure as well as the fraction of each intermetallic phase in Al matrix, and details are summarized in Table 5–4. These results will be used later in modeling the shielding behavior of steel-steel CMFs against neutrons.

Table 5–3: Chemical Compositions and calculated solid density of intermetallic phases in Al-steel CMFs (wt %)

	Al	Si	Fe	Cr	Mn	Solid Density ρ_s (g/cm^3)
Intermetallic layer	58.52%	6.74%	27.57%	6.39%	0.78%	4.42
Plate shape	60.59%	8.17%	22.78%	7.51%	0.95%	4.23
Needle shape	72.60%	5.02%	21.53%	0.85%	0.00%	3.83

Table 5–4: Physical parameters of Al-steel CMFs

Al-steel CMFs	Matrix porosity (%)	Matrix density (g/cm^3)	Thickness of intermetallic layer (μm)	Density of intermetallic layer (g/cm^3)	vol % of plate shape precipitation	Density of plate shape precipitation (g/cm^3)	vol % of needle shape precipitation	Density of needle shape precipitation (g/cm^3)
2.0mm	34.01	1.78	37.90±0.91	2.92	11.21	2.79	4.36	2.53
4.0mm	6.74	2.52	110.89±10.20	4.12	23.57	3.94	10.02	3.57
5.2mm	18.44	2.20	10.01±0.20	3.61	13.28	3.45	3.71	3.13

This result made us believe that there may be a correlation between the neutron shielding of Al-steel CMFs and the percentage of intermetallic phases around spheres and within the matrix. Upon further investigation, we found out that there was no particular relations between the neutron shielding and the formation of intermetallics in the matrix of aluminum-steel CMFs. As the result, the slight difference between the performance of 4 mm sphere Al-steel CMF and other samples are simply related to the slightly higher t/r ration of spheres.

A New Light Weight Structural Material for Nuclear Structures

Open-cell Al foam with fillers

For a neutron of kinetic energy E encountering a nucleus of atomic weight A, the average energy loss can be expressed as $2EA/(A+1)^2$. The average energy loss reaches its largest value of E/2 by using hydrogen (A=1). As shown in Fig 5b, open-cell Al foams with various fillers exhibited strong hydrogen dependency on attenuating neutrons. Open-cell Al foam + wax are measured to be more efficient than open-cell Al foam + water due to higher hydrogen content. It should be noticed that open-cell Al foam + PE with a hydrogen content of 11.6 wt% offers better neutron shielding effectiveness than that of open-cell Al foam + wax with a hydrogen content of 14.8 wt% (Table 3–4). This may be attributed to the presence of an additional 5 wt% of boron in PE (Table 3–4). After being scattered by a nucleus, the neutron may be absorbed or captured by an absorber. Boron is one of the most commonly used neutron absorbers owing to its large absorption cross section. Similarly, open-cell Al foam + borated water presented an improvement on neutron shielding compared to open-cell Al foam + water as a result of the additional of only 0.1 wt% boron content.

5.4   Mechanical properties of Composite Metal Foams

The compressive stress-strain relationships of (4mm sphere) S-S CMF and (4mm sphere) HZ S-S CMF subjected to quasi-static loading are shown in Figure 5–12. It can be seen that these two CMFs have similar stress-strain behavior that includes three distinct regions: (I) a linear elastic region appears at a low strain, (II) A plateau region covers up to over 50% strain and (III) a densification which is following the plateau region after 50% strain. During the plateau region all of the spheres and porosities in the material are gradually collapse through a large irreversible plastic deformation along with a slight increase in stress value. However, the stress increases drastically with slight increase of strain in densification region. Both (4mm sphere) S-S CMF and (4mm sphere) HZ S-S continue a uniform deformation from the early stage of the compression to the higher strains, no evidence of visible collapse bands were observed in specimen. The deformation of (4mm sphere) HZ S-S CMF under quasi-static loading condition is shown in Figure 5–13. It can be clearly seen that the material maintains its integrity and uniform deformation throughout the entire compression process. A slightly decrease in the plateau stress, from 127MPa of (4mm sphere) S-S CMF to 114MPa of (4mm sphere) HZ S-S CMF, can be observed. This is resulted from the decrease of the specimen density from 3.2g/cm^3 ((4mm sphere) S-S CMFs) to 2.9g/cm^3 ((4mm sphere) HZ S-S CMF). The density decrease might be linked with the slightly lower sintering temperature of (4mm sphere) HZ S-S CMF (Figure 5–14a, indicated in red arrows), which could have caused the remaining of some un-sintered particles in the material. As a result, some irregular micro-porosities appeared within the matrix of HZ S-S CMF. Whereas in (4mm sphere) S-S CMF (Figure 5–14b), matrix materials are very well sintered, no micro-porosities occurred. The results of this work indicate that by adding small amount of high-Z elements such as Tungsten into the matrix of CMFs, not only we have maintained the mechanical strength and energy absorption of the material, but also its shielding against X-ray, gamma and neutron was drastically improved. This research opens up room for further investigation to optimize the best way of utilizing the composite metal foams in nuclear structures.
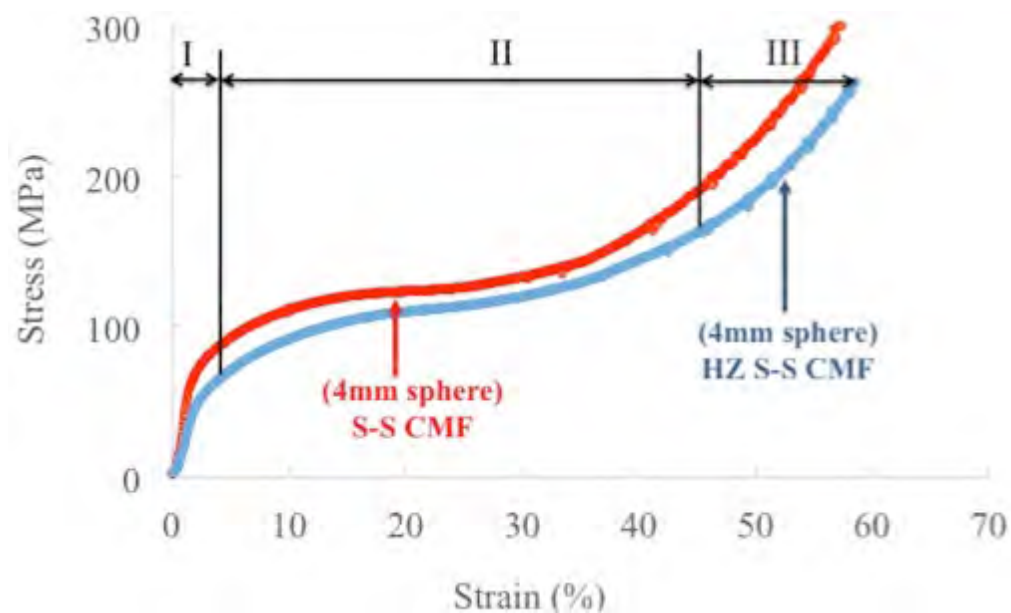
Figure 5–12: Stress-strain curves of 4mm steel spheres in Stainless steel matrix or in a high-Z matrix of CMF
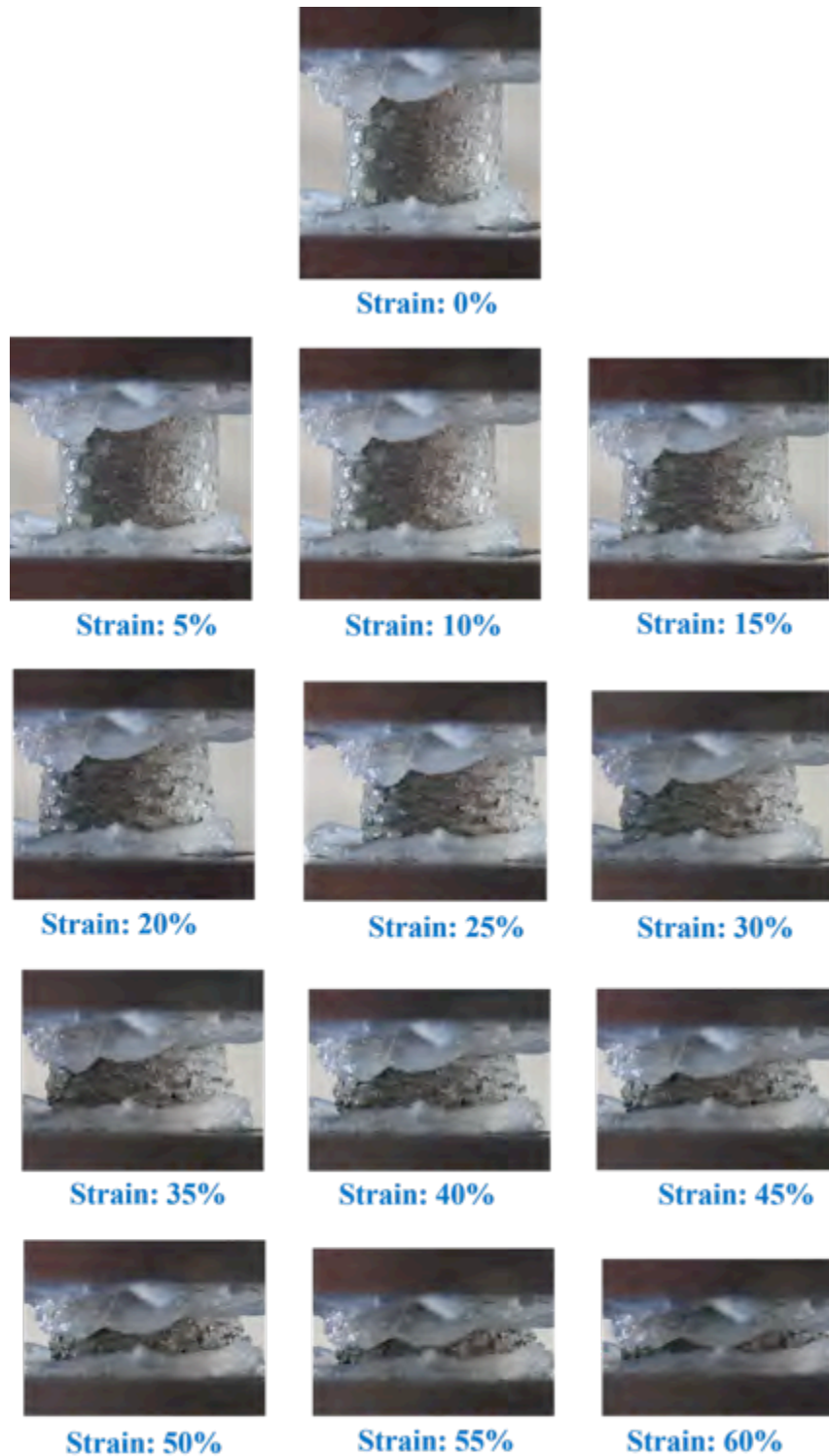
Figure 5–13: Sequential images showing the deformation of (4mm sphere) HZ S-S CMF under quasi-static loading. The white area on the top and bottom are vacuum grease used for lubrication.
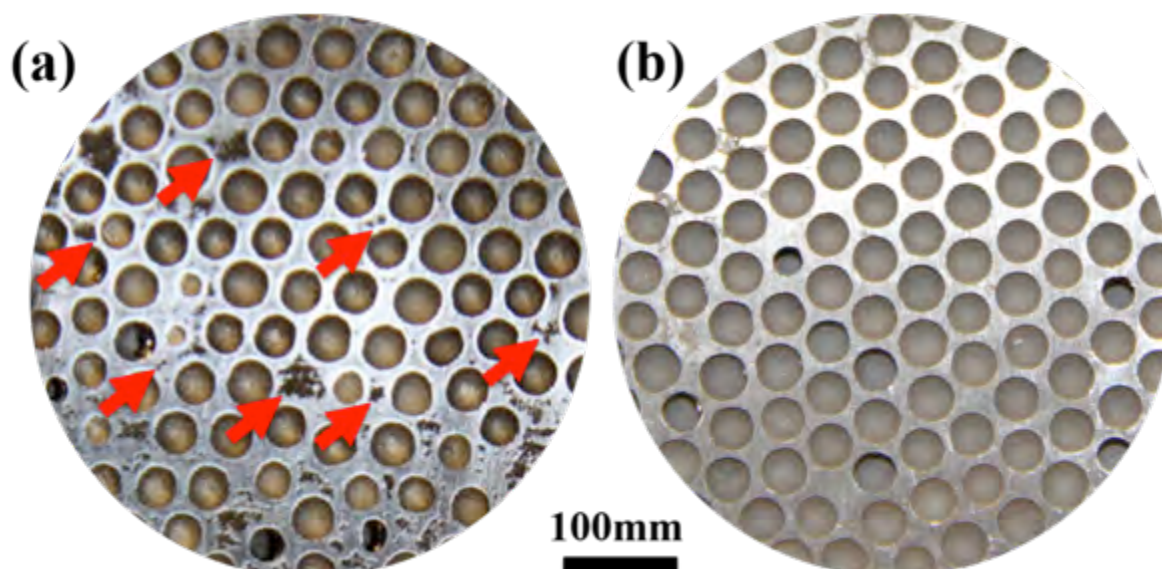
Figure 5–14: Digital images showing the cross-section cut of (a) (4mm sphere) HZ S-S CMF, and (b) (4mm sphere) S-S CMF before quasi-static testing. Red arrows indicate the micro-porosity among (4mm sphere) HZ S-S CMF matrix

5.5   Thermal properties of CMFs

5.5.1   Effective thermal conductivity

Thermal conductivity data for control materials: 316L stainless steel and Aluminum A356 are available in literature as a source of comparison [25] . Table 5–5 and Table 5–6 summarize effective thermal conductivity values of CMFs and control materials, respectively.

Figure 5–15 shows temperature-dependent thermal conductivities of CMFs, and two control materials. Both Al-S CMF and S-S CMF exhibit much lower thermal conductivity than their bulk matrix material. This is due to the presence of the hollow spheres within the matrix. In thermal conductivity studies, the void plays an important role due to the lowest thermal conductivity of air inside them [26]. Thus, the high air content inside CMFs offers extremely good thermal insulation performance as compared to the commercially available nuclear structural material such as Aluminum and stainless steel.

Table 5–5: Experimental and theoretical values of effective thermal conductivities for (2mm sphere) S-S CMF, (4mm sphere) S-S CMF, and (4mm sphere) Al-S CMF

Material Description	Nominal temperature (°C)	Actual temperature (°C)	Experimental thermal conductivity (W/m-K)	Brailsford and Major's model (W/m-K)	Difference between experimental and theoretical results (100%)
(2mm sphere) S-S CMF	300	301	3.9±0.20	4.5	16
	400	402	4.4±0.22	5.1	15
	500	503	5.0±0.25	5.6	12
	600	605	5.6±0.28	6.1	9
(4mm sphere) S-S CMF	300	302	3.8±0.19	4.7	22
	400	402	4.4±0.22	5.2	20
	500	503	5.0±0.25	5.8	16
	600	605	5.7±0.29	6.4	11
(4mm sphere) Al-S CMF	300	301	32.1±1.61	36.9	15
	400	402	30.7±1.84	38.9	27
	500	503	30.3±1.52	38.4	27

Table 5–6: Thermal conductivities of 316L stainless steel, Aluminum A356, and air

Material Description	Temperature (°C)	Thermal conductivity (W/m-K)
316L stainless steel	300	13.4
	400	15.2
	500	16.8
	600	18.4
Aluminum A356	300	205
	400	215
	500	210
Air	300	0.0451
	400	0.0510
	500	0.0564
	600	0.0615

It is well-known that Aluminum exhibits very high heat conductivity, which is governed by behavior valence electrons [27] . As shown in Table 5–6, thermal conductivity of Aluminum A356 is about fourteen times higher than that of 316L stainless steel. However, the difference between S-S CMF and Al-S CMF is relatively small, where the thermal conductivity of Al-S CMF is seven times higher than that of S-S CMF. This is attributed to the placement of hollow steel spheres within Al matrix in Al-S CMF, the sphere wall material and air inside sphere core have lower thermal conductivity compared to Al. Another contribution might be resulted from the additional voids within the Al matrix. Figure 5–10 shows the voids between spheres. The unfilled portion may act as heat resistance to decrease the conductivity. (2mm sphere) and (4mm sphere) S-S CMFs have shown similar thermal conductivity at a given temperature (Table 5–5).

This is due to the fact that the sphere wall thickness to its diameter ratio is almost the same in all various sphere sizes and as such there is the same amount of sphere and matrix materials in various samples. All of these can be translated into a similar volume fraction of spheres wall and matrix material in all samples (Table 5–7). Therefore, the thermal conductivity of S-S CMF is relatively independent of sphere size. It should be noted that the variation of thermal conductivity of S-S CMFs is relatively small under the measured temperature range comparing with solid stainless steel. Stable thermal conductivity of CMFs under high

temperature is important for their practical application, which is closely related to the life and reliability of nuclear structural applications.

Table 5–7: Volume fraction of sphere wall material, matrix material, and air in CMFs

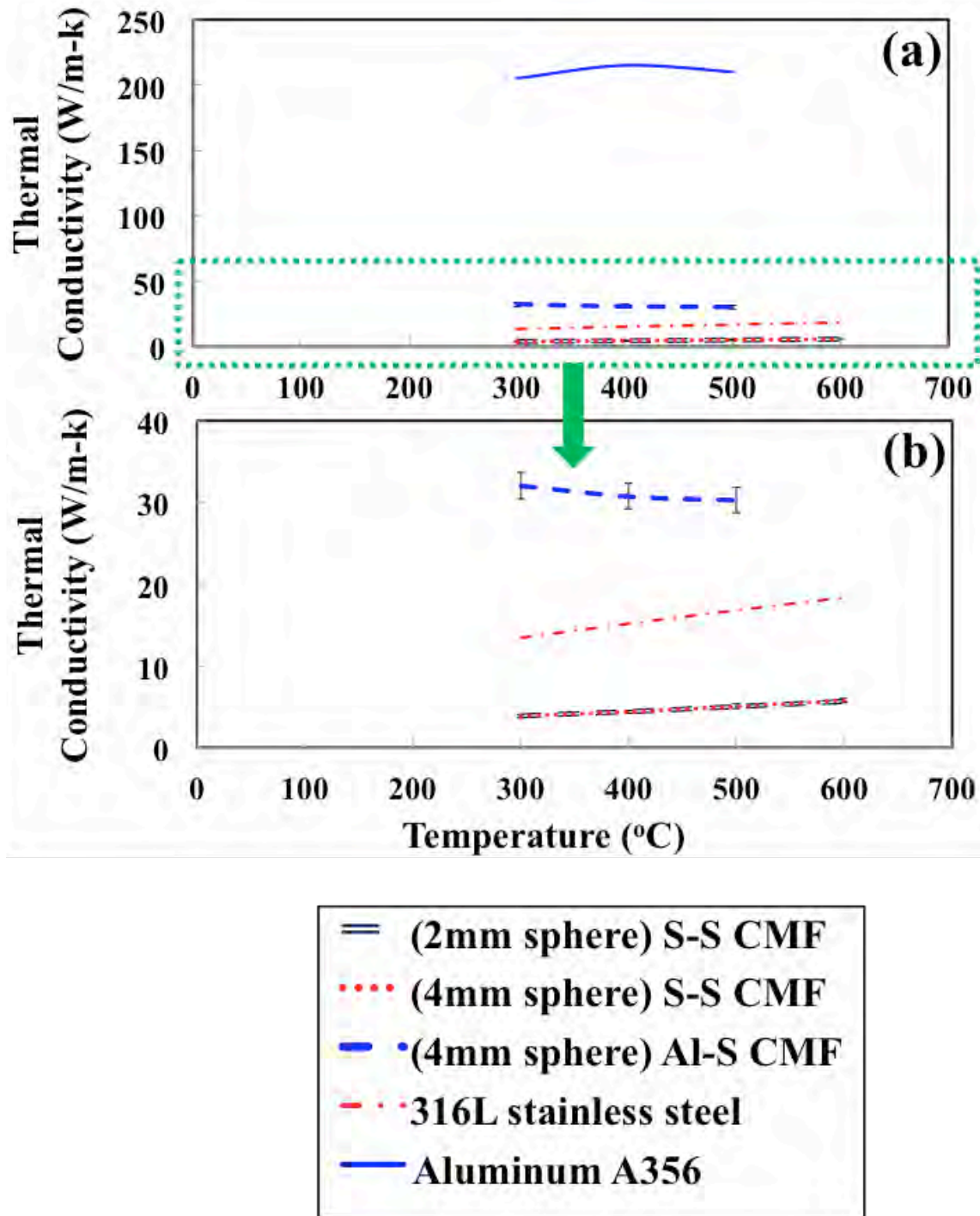| Samples	Volume fraction of matrix material (vol%)	Volume fraction of sphere wall material (vol%)	Volume fraction of sphere core (vol%)	Radius ratio of steel hollow sphere (η)
(2mm sphere) S-S CMF	28.4	15.0	56.6	0.898
(4mm sphere) S-S CMF	25.4	16.5	58.0	0.873
(4mm sphere) Al-S CMF	23.2	16.5	60.2	0.873

Figure 5–15: Thermal conductivity as a function of temperature for (a) all testing samples, and (b) zoomed in section related to CMF samples and 316L stainless steel control sample

A New Light Weight Structural Material for Nuclear Structures

Brailsford and Major [28] developed a model for the effective thermal conductivity of monodisperse homogeneous particles made of two different materials randomly distributed in a continuous matrix. They compared the experimental results with the relation derived from their study, and a good agreement was obtained. The effective thermal conductivity $\left(k_{eff}\right)$ of three-component media is given by (Brailsford and Major, 1964):

$$k_{eff} = \frac{k_m\phi_m + k_{sc}\phi_{sc}\dfrac{3k_m}{\left(2k_m + k_c\right)} + k_{sw}\phi_{sw}\dfrac{3k_m}{\left(2k_m + k_c\right)}}{\phi_m + \phi_{sc}\dfrac{3k_m}{\left(2k_m + k_c\right)} + \phi_{sw}\dfrac{3k_m}{\left(2k_m + k_c\right)}} \tag{17}$$

where k_m, k_{sw}, and k_{sc} are the thermal conductivities of the matrix, sphere wall, and sphere core materials, respectively. Similarly, ϕ_m, ϕ_{sw}, and ϕ_{sc} are the volume fractions of the matrix, sphere wall, and sphere core materials, respectively.

The theoretical effective thermal conductivity was obtained by using Brailsford and Major's model [28] and compared with experimental results in Table 5–5. Notwithstanding some hypotheses and simplifications have been proposed in order to construct Brailsford and Major's model, the analytical results show a good agreement with the experimentally measured thermal conductivity. The effective thermal conductivities of (2mm sphere) S-S CMF, (4mm sphere) S-S CMF, and (4mm sphere) Al-S CMF were experimentally studied by means of high temperature guarded-comparative-longitudinal heat flow technique, and theoretically verified by Brailsford and Major's model. It was observed that both Al-S CMF and S-S CMF possess lower effective thermal conductivity than their matrix bulk material. In S-S CMF, the effective thermal conductivity is relatively independent of the sphere size owing to the similar volume fraction of sphere wall material, matrix material, and air in all CMF samples.

The CMFs developed and discussed in this work offer extremely good thermal insulation performance to weight ratio as compared to many commercially available nuclear structural material such as Aluminum and stainless steel. This work not only highlights the outstanding performance of composite metal foams as a lightweight material with good radiation attenuation, but also their outstanding thermal insulation capability. This unusual phenomenon may open doors to many future applications of CMFs.

5.5.2 Coefficient of thermal expansion results and discussions

The thermal strain of (2mm sphere) S-S CMF and (4mm sphere) S-S CMF were measured in temperature range of 0-400°C and presented in Figure 5–16. It was observed that (2mm sphere) and (4mm sphere) S-S CMFs exhibit very similar behavior, their thermal strain increase linearly with increasing of the temperature. The linear increment may be attributed to the similar matrix and spheres wall material; both sphere wall and matrix are made of stainless steel, there is no induced thermal stress during the heating process. The sphere size effect on Coefficient of Thermal Expansion (CTE) is relatively small, which may be resulted from their similar volume fraction of sphere wall material, matrix material, and air (Table 4–1). CTE values were calculated to be 3×10^{-6} $°C^{-1}$ for both S-S CMFs with various sphere sizes. These experimental results are listed in Table 5–9, and plotted in Figure 5–17 in comparison with 316L stainless steel control material.
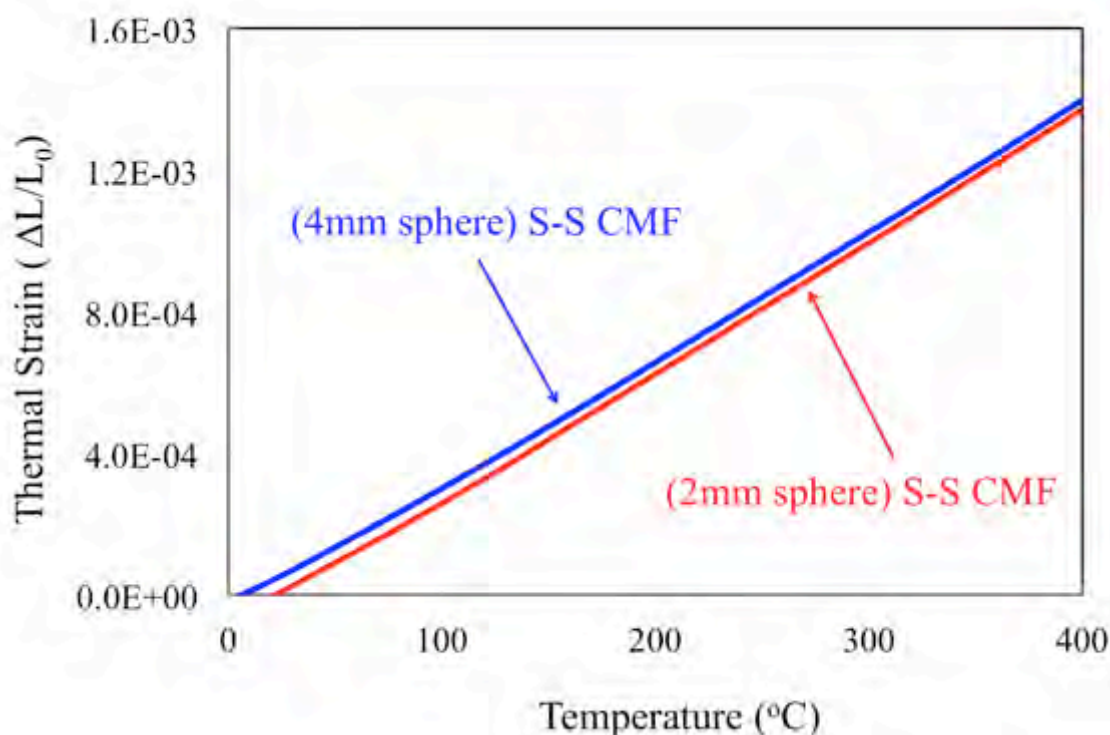
Figure 5–16: Thermal strain of (2mm sphere) S-S CMF and (4mm sphere) S-S CMF as a function of temperature
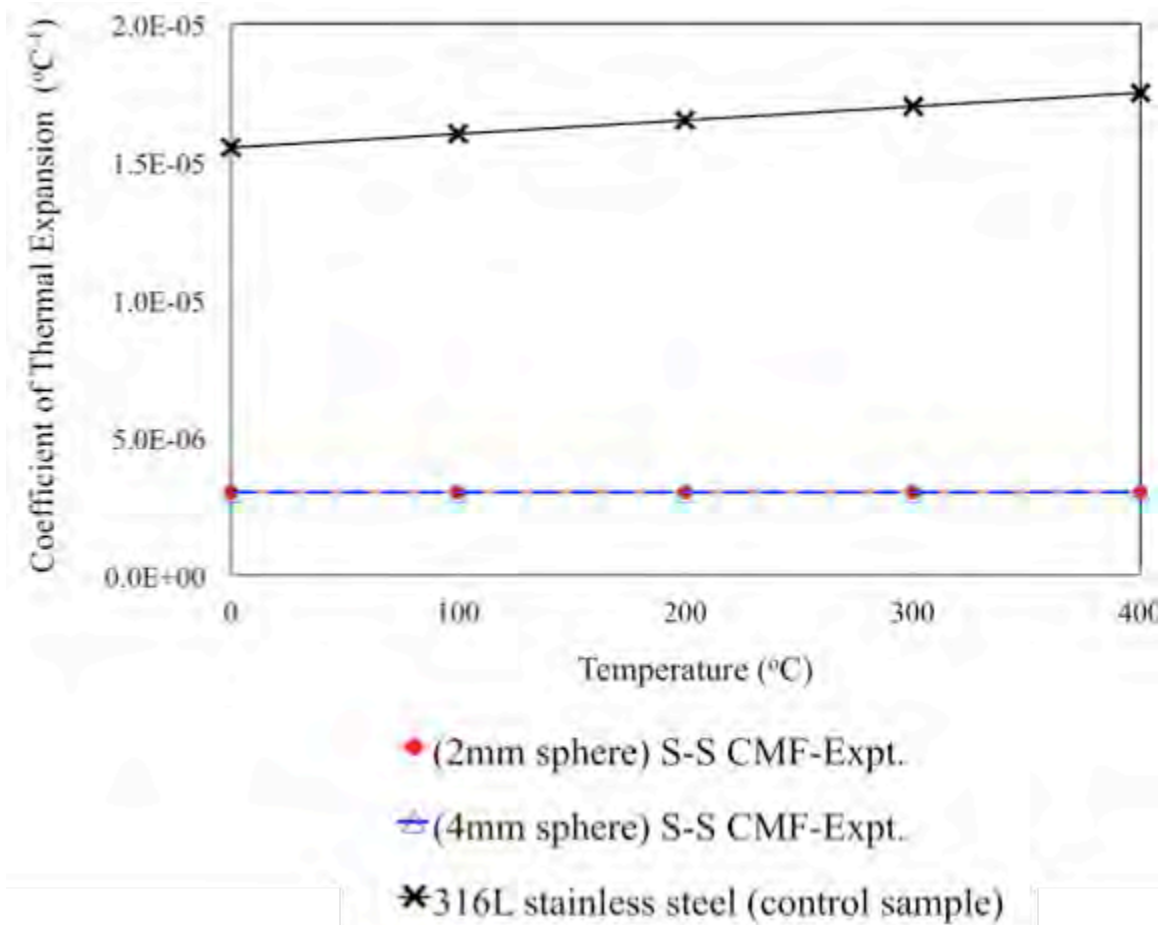
Figure 5–17: Experimental coefficient of thermal expansion of CMFs as compared with 316L stainless steel

It is interesting to observe that S-S CMF display superior thermal stability, its CTE was constant over the testing temperature range (0-400°C). For the structural materials used in nuclear applications, high degree of dimensional stability with temperature fluctuations is very essential in order to minimize the possibility of failure induced by thermal stress. As compared to 316L stainless steel, it can be clearly seen that the addition of steel hollow spheres into stainless steel matrix in S-S CMF resulted in a decrease in CTE by about 80% compared to bulk stainless steel. This 80% reduction is achieved by adding 59% volume fraction of steel hollow sphere into the matrix. The relations between the CTE of CMFs and various material parameters such as matrix/sphere/air volume fraction, matrix/sphere materials need to be further developed to obtain a quantitative understanding of these parameters.

Table 5–8: Experimental and theoretical values of coefficient of thermal expansions for (2mm sphere) S-S CMF and (4mm sphere) S-S CMF

Material Description	Temperature (°C)	Experimental CTE (°C^{-1})	Theoretical CTE (°C^{-1})	Difference between experimental and theoretical results (%)
(2mm sphere) S-S CMF	0	3.00E-06 ±0.03E-06	2.47E-06	18
	100		2.50E-06	17
	200		2.57E-06	14
	300		2.63E-06	12
	400		2.78E-06	7
(4mm sphere) S-S CMF	0	3.00E-06 ±0.20E-06	2.52E-06	16
	100		2.58E-06	14
	200		2.63E-06	12
	300		2.79E-06	7
	400		2.83E-06	6

Table 5–9: Physical properties of 316L stainless steel for thermal expansion prediction

Material Description	Temperature (°C)	Mean CTE (°C^{-1})	Young's modules (GPa)	Poisson's ratio	Effective modulus of 2mm sphere (GPa)	Effective modulus of 4mm sphere (GPa)
316L stainless steel	0	1.55E-05	200	0.20	23.41	28.34
	100	1.60E-05	194	0.24	19.75	23.90
	200	1.65E-05	186	0.27	16.76	20.28
	300	1.70E-05	179	0.32	12.58	15.23
	400	1.75E-05	172	0.32	12.09	14.63

http://www.bssa.org.uk/topics.php?article=139

The CTE of CMFs is relatively difficult to predict precisely because it is influenced by several factors including matrix plasticity and the internal structure of the material, which typically consists of hollow particles embedded in a continuous metallic matrix. CMFs used in this work are random and isotropic. The most often used is Turner's model, which is given by [29]:

$$\alpha_{CTE} = \frac{\alpha_m \phi_m K_m + \alpha_s \phi_s K_s}{\phi_m K_m + \phi_s K_s} \qquad (18)$$

where α_m and α_s are the CTE of the bulk matrix and sphere, respectively. Similarly, ϕ_m and ϕ_s are volume fraction of the matrix and sphere, respectively, while K_m and K_s are the bulk moduli of the matrix and sphere, respectively.

The bulk modulus can be estimated from the Young's modulus (E) of the constituents as:

$$K = \frac{E}{3(1-2v)} \qquad (19)$$

where (v) is the Poisson's ratio of the respective constituents

Turner's model is mainly applicable to composites containing solid fillers and do not include particle wall thickness, which is an additional parameter in CMFs. In order to determine the effective steel hollow sphere modulus, the radial displacement at the outer surface of the two systems are compared and the effective modulus (E^*) as a function of the hollow sphere radius ratio is found as [30]:

$$E^* = \frac{E_{sw}(1-2v)(1-\eta^3)}{(1-2v)+\frac{(1+v)\eta^3}{2}} \qquad (20)$$

where (E_{sw}) is the modulus of the sphere wall material and it can be found in Table 5–9. The modified Turner's model for CTE of hollow particle filled composites is given by substituting Equation 19 and Equation 20, into Equation 18 as [14]:

$$\alpha_{CTE} = \frac{\alpha_m \phi_m E_m \left[(1-2v_{sw}) + \frac{(1+v_{sw})\eta^3}{2} \right] + \alpha_s \phi_s E_{sw}(1-2v_m)(1-\eta^3)}{\phi_m E_m \left[(1-2v_{sw}) + \frac{(1+v_{sw})\eta^3}{2} \right] + \phi_s E_{sw}(1-2v_m)(1-\eta^3)} \qquad (21)$$

The values of (η) is defined as radius ratio (Gupta et al., 2010):

$$\eta = \frac{r_i}{r_o} \qquad (22)$$

where r_i and r_o are the inner and outer radii of the hollow sphere. The calculated values of are listed in Table 5–7.

The comparison of theoretical and experimental values for CTE of CMFs at various temperatures is shown in Table 5–8. Good matching between theoretical and experimental results can be observed. In order to increase the precision and the reliability of the modeling, further microstructural studies to more precisely characterize the volume fractions of the matrix, sphere wall and air, as well as sphere distribution and inner and outer radius ration are required. The CTE of (2mm sphere) S-S CMF and (4mm sphere) S-S CMF was experimentally measured using thermomechanical analyzer (TMA), and verified through modified Turner's model. The CTE of CMFs was observed to be 80% lower than the matrix material, 316L stainless steel. The sphere size effect is relatively small in S-S CMF due to the similar volume fraction of the sphere and matrix material in the material. The most important finding is that S-S CMF possesses superior thermal stability under high temperature condition, this is a desirable characteristics for the materials used in nuclear facilities. In the applications such structural material in spent fuel cask, high degree of dimensional stability with temperature fluctuations is very essential to prevent structural failure induced by thermal stress. The experimental trends were analyzed by using Turner's model modified for CMFs. The results from the modified Turner's model show close correlation with the experimental values with a mean difference of 9 %.

The experimental observations are limited due to the number of samples tested in this work. The relations between the CTE of CMFs and various material parameters such as matrix/sphere/air volume fraction, matrix/sphere materials, wall thickness, and all variables are of interest to study in future work to obtain a quantitative understanding of these parameters on thermal performance of the material. These relations can help in engineering lightweight CMFs for nuclear structural applications where component material having a specific CTE value is required.

5.6   Flame test experimental results and discussions

Sequential IR images of (2mm sphere) S-S CMF and 304L stainless steel are both displayed in Figure 5–18. As can be seen, 304L stainless steel reached its thermal steady state in about 4mins, while it took 8mins for S-S CMF to reach its equilibrium condition. The main reason for flame retardant function of CMF is associated with the high percentage of porosity (about 60%) filled with low heat permeability air, which restrict fire and prevent the heat transfer.

Whereas in solid 304L stainless steel, there is no air and the heat spreads quickly. As such the S-S CMF seems to preform better under nuclear waste flame test conditions.

A physics-based three-dimensional model accounting for the conduction of materials was carried out using finite element analysis in ANSYS WorkBench. The sphere packing arrangement in (2mm sphere) S-S CMF is represented through body-centered cubic (BCC). The boundary conditions implemented in the thermal model are based on the experimental setup, where the top and side faces are thermally insulated. The model is subjected to a 25.4mm diameter heat source held at a constant temperature of 800°C at the bottom to mimic the heat input from the flame. The heat convection and radiation through the sphere pores are neglected since their outer diameters are only 2 mm. It has been shown that the convection has negligible effects in hollow spheres with diameters less than 4 mm [31] . In addition, the flux due to radiation typically does not control heat transfer in composite foams. As such, this study only considers conduction to model the flame retardant behavior of CMF. In order to fully compare the model with bulk stainless steel, custom inputs for the three-dimensional model including density, specific heat, and thermal conductivity, taken from the experimental results. The geometry was created by introduction of porosities arranged in Body Centered Cubic structure with an inner diameter of 1.9 mm in the matrix. Both spheres and matrix are considered as one material, assuming uniform chemical composition, grain structure, and microporosities.

A side view of the model for the flame test of (2mm) S-S CMF and 304L stainless steel is shown in Figure 5–19. The model seems to be in good agreement with the experimental results. Variation between the model and the experiment can be attributed to initial assumptions made when creating the model such as the perfect bonding between spheres and matrix and a uniform distribution of chemical composition, uniform grain sizes and porosity content in sphere walls and matrix as well as the assumed heat source size and shape. The model can be further expanded upon future analysis by differentiating the sphere and matrix.
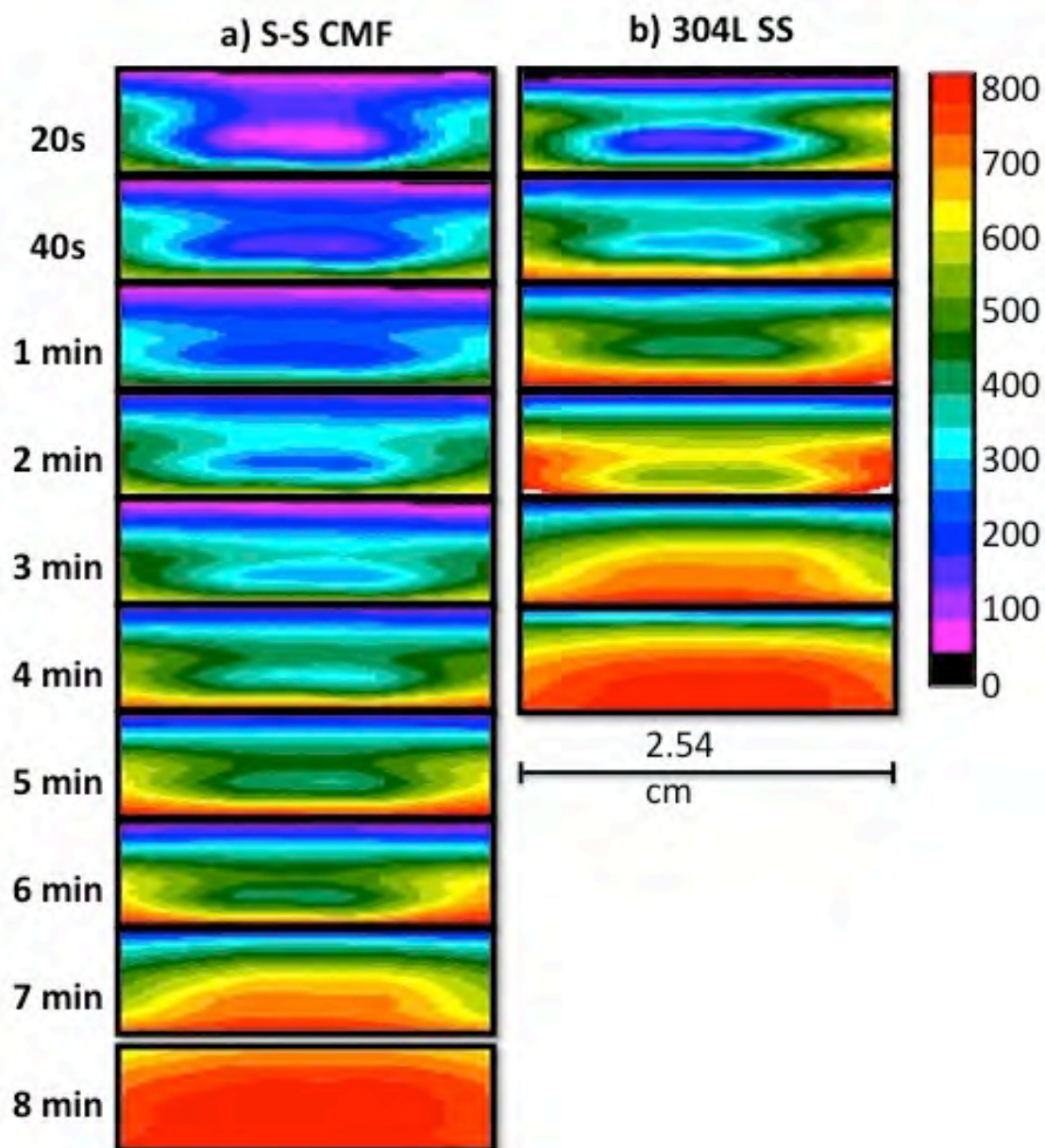
Figure 5–18: Sequential IR images showing temperature profile of a) (2mm sphere) S-S CMF and b) 304L stainless steel during flame test exposed to an 800ºC flame
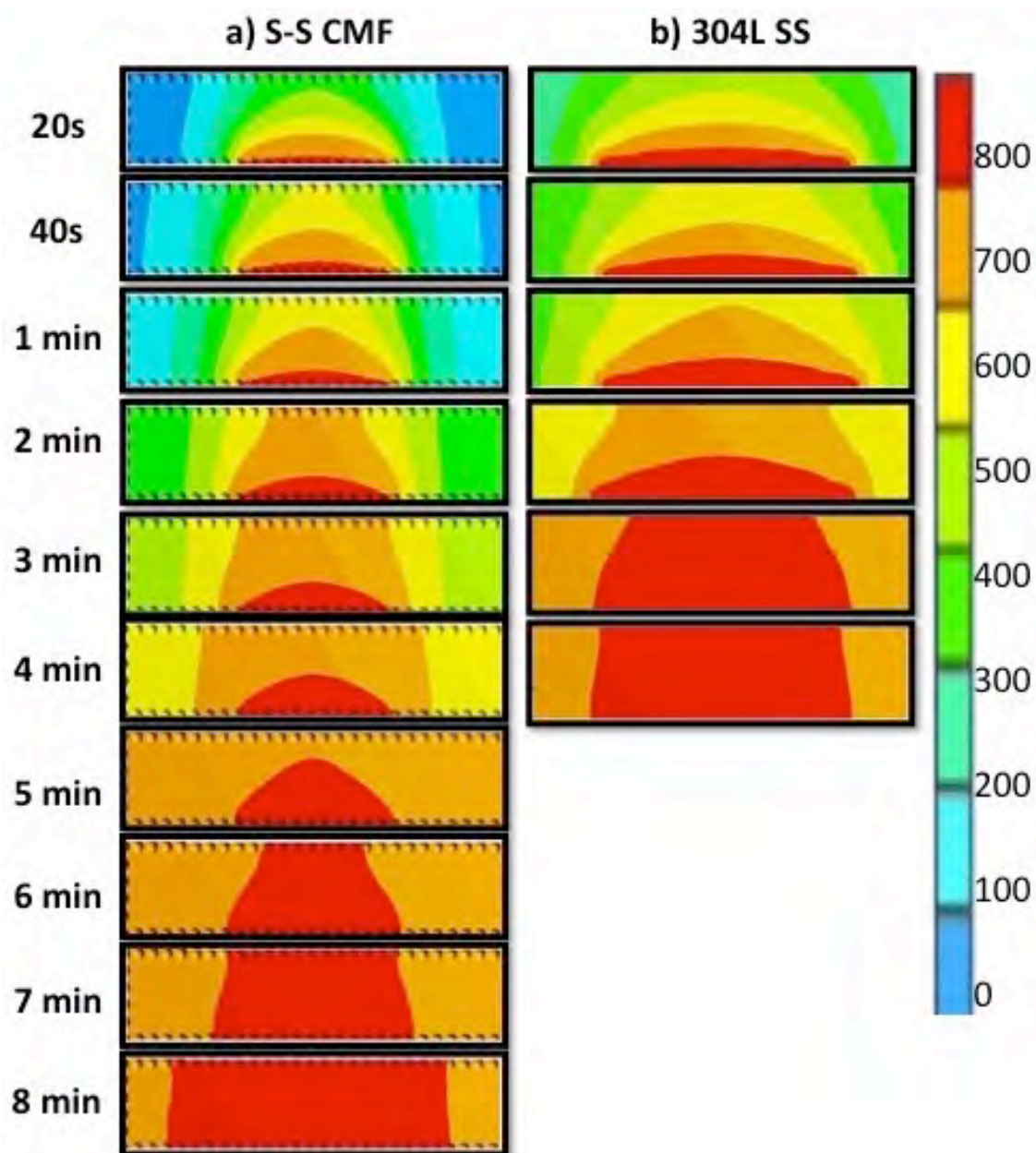
Figure 5–19: Finite element analysis modeling with center section view of a) (2mm sphere) S-S CMF and b) 304L stainless steel exposed to an 800ºC flame at the base.

A New Light Weight Structural Material for Nuclear Structures

CHAPTER 6   MODELING AND SIMULATIONS

6.1   XCOM analyses for X-Ray transmission

In Table 6–1, the mass attenuation coefficient was computed using experimentally measured X-ray transmission and theoretically obtained mass attenuation coefficient values using XCOM. As can be seen the experimental and theoretical data are in good agreement. The over-all uncertainty could be determined by errors in areal density measurements and counting statistic, as well as non-homogeneous porous structure of samples and the resulting multiple scattering.

Table 6–1: Mass attenuation coefficient of CMFs, Aluminum A356 and lead at X-ray energy of 100 kVp

Samples	Experimental	Theoretical
(2mm sphere) S-S CMF	0.4053±0.0059	0.3477
(2mm sphere) Al-S CMF	0.2089±0.0024	0.2498
(4mm sphere) S-S CMF	0.4044±0.0084	0.3474
(4mm sphere) HZ S-S CMF	0.9517±0.0090	0.9416
(4mm sphere) Al-S CMF	0.2081±0.0023	0.2503
(5.2mm sphere) S-S CMF	0.4044±0.0027	0.3474
(5.2mm sphere) Al-S CMF	0.2081±0.0025	0.2499
Aluminum A356	0.1494±0.0062	0.1572
Lead	4.985±0.0016	5.336

6.2   XCOM Analyses for Gamma Ray Transmission

Theoretical mass attenuation coefficients were determined using XCOM code with photon energy ranging from 0.01MeV to 10MeV. The weight fraction (wt %) of each element in each material was used as an input. The comparison of measured mass attenuation coefficients with theoretical values are summarized in Table 6–2 and plotted as a function of photon energy in Figure 6–1. As listed in Table 6–2, the experimentally measured values are in good agreement with the theoretically calculated values within acceptable experimental errors. It should be noted that, the discrepancy between experimental and theoretical values for thicker steel-steel CMF is

as the result of an early termination of the experiment due to the complete attenuation of for ^{241}Am. The unique non-homogenous structure of metal foams also contributes to the difference between the measured and theoretical values. Therefore, the mean difference was estimated to be 7.01% with the major contributors arising from the uncertainty of sample impurity and non-uniformity, error in evaluation of sample thickness and areal density. Other contributions originate from deviations of narrow beam geometry, counting statistical, the small angle scattering contribution, and the effects of multiple scattering. It is clearly seen from Figure 6–1 that the experimental values fall onto the theoretical curve computed by XCOM code and show a good agreement within the experimental error, and increasing photon energy causes the decrease in mass attenuation coefficient; initially the mass attenuation coefficient is in its maximum value, and it drops rapidly with increasing the photon energy for all six sets of samples up to 0.01MeV.
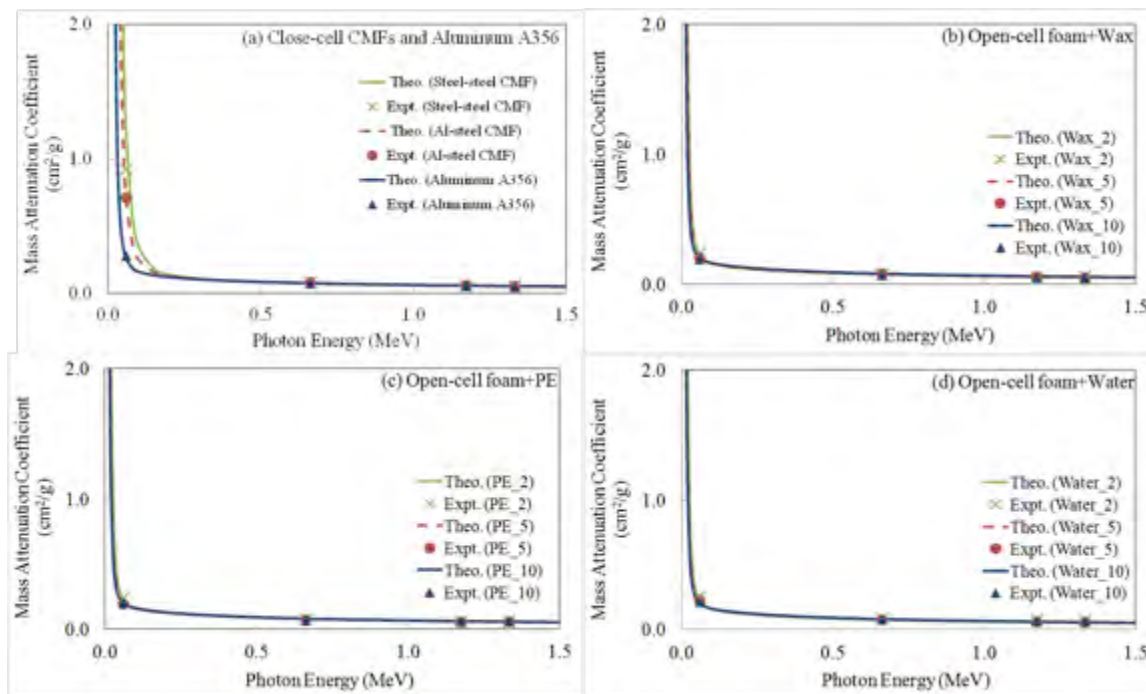
Figure 6–1: Comparison of experimental and theoretical mass attenuation coefficients of (a) Close-cell CMFs and Aluminum A356, (b) open-cell foam + Wax, (c) open-cell foam + PE, and (d) open-cell foam + Water as a function of photon energy

Steel-steel CMF shows maximum value for mass attenuation coefficient among all samples, the mass attenuation coefficients of steel-steel CMF and Al-steel CMF under ^{241}Am source are measured 400% and 300% higher than that of Aluminum A356 respectively. This may be attributed to the fact that close-cell CMFs contain large amounts of relatively high

atomic number constituent elements with ^{26}Fe (65.72%) and ^{24}Cr (17.13%) for steel-steel CMF and ^{26}Fe (32.24%) and ^{13}Al (47.29%) for Al-steel CMF, for which photoelectric effect is a dominating factor and hence energy attenuation is higher. Open-cell Al foam with fillers, on the other hand, contains large amounts of low atomic number constituent elements such as ^{8}O, ^{6}C, and ^{1}H, and hence they have lower energy attenuation. These low Z elements are very effective for neutron attenuation as reported in our previous chapter.

6.3   MCNP Simulation for Neutron Transmission

Simulation was conducted through Monte Carlo N-Particle Transport Code version 5 (MCNP5) in order to test the accuracy of the experimental results. In MCNP5 codes, the experimental setup follows narrow beam transmission geometry as described in Section 3. Tally F4 was used to obtain simulation data. This tally scores neutron flux in the detector cell. Simulations were performed with 10^6 histories. All the data obtained by MCNP5 were reported with less than 0.5% error. Figure 6–2 shows modeled close-cell CMF samples, collimated beam source energy, source position and dosimetric volume in this simulated geometry.

Table 6–2: Experimental and theoretical values of mass attenuation coefficients (cm^2/g) for close-cell CMFs and Aluminum A356 at four different photon energies

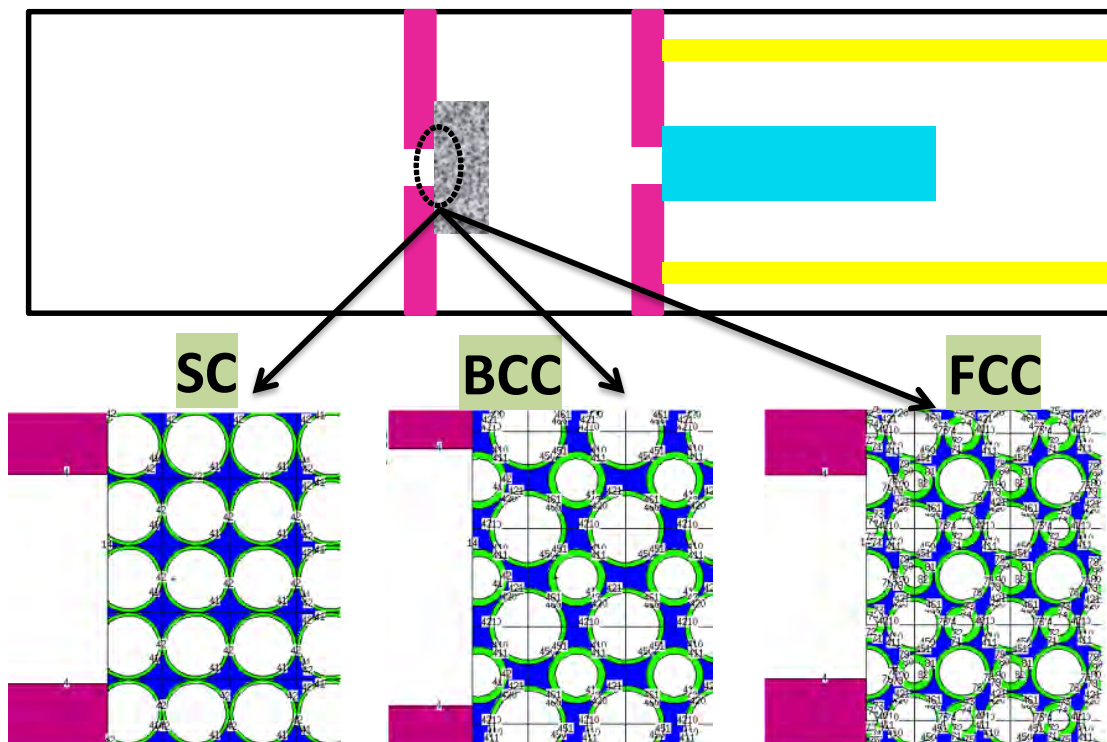| Source	Energy (MeV)	Steel-steel CMF		Al-steel CMF		Aluminum A356	
		Expt.	Theo.	Expt.	Theo.	Expt.	Theo.
^{60}Co	1.332	0.0524 ±0.0038	0.0516	0.0481 ±0.0041	0.0525	0.0489 ±0.0036	0.0532
^{60}Co	1.173	0.0525 ±0.0035	0.0550	0.0561 ±0.0035	0.0559	0.0549 ±0.0029	0.0568
^{137}Cs	0.662	0.0806 ±0.0025	0.0726	0.0779 ±0.0025	0.0736	0.0733 ±0.0025	0.0745
^{241}Am	0.060	**0.9195 ±0.0062**	**1.1683**	**0.7112 ±0.0024**	**0.6937**	**0.2773 ±0.0023**	**0.2556**

Figure 6–2: Geometry of modeled configuration close-cell CMFs

6.3.1 Modeling of close-cell CMFs

A 3D model was built by using MCNP5 code to evaluate neutron interaction with close-cell CMFs. The hollow sphere packing density of close-cell CMFs was reported to be 0.59 [11], which is classified as random loose packing. In order to simplify the complex structure of close-cell CMFs, sphere packing arrangement was represented through three structures: simple cubic (SC), body centered cubic (BCC) and face centered cubic (FCC), with packing factor of 0.52, 0.68, and 0.74, respectively. Lattice parameter of each structure can be then calculated through $a_{SC} = 2R$, $a_{BCC} = 4R/\sqrt{3}$, and $a_{FCC} = 4R/\sqrt{2}$, where R is sphere outer radius. While the steel-steel CMFs is easier to model, Al-steel CMFs is much more complicated due to the presence of different sphere wall and matrix materials, the presence of intermetallic layer around the sphere wall as well as plate shape and needle shape precipitations in the matrix, which needed to be incorporated into the model. As a result, while R is only the outer radius of spheres in steel-steel CMFs, it is modified to be the sum of sphere outer radius plus the thickness of intermetallic layer in Al-steel CMFs. Plate shape and needle shape precipitations were represented by respectively

cubical and cylindrical elements that are evenly distributed within Al matrix. The size and shape of these phases were estimated through image J and summarized in Table 6–3 and

Table 6–4. The material properties for various components in the model can be found in Table 3–1 and Table 3–2.

Table 6–3: Characteristics of SC, BCC, and FCC structures in MCNP5 modeling for steel-steel CMFs

		Lattice parameter a (cm)		
		SC	BCC	FCC
	2.0mm	0.20	0.23	0.28
Steel-steel CMFs	4.0mm	0.40	0.46	0.57
	5.2mm	0.52	0.60	0.74

Table 6–4: Characteristics of SC, BCC, and FCC structures in MCNP5 modeling for Al-steel CMFs

		Lattice parameter a (cm)			Plate shape precipitation (µm)	Needle shape precipitation (µm)	
		SC	BCC	FCC	Lattice parameter	Diameter	Length
	2.0mm	0.21	0.24	0.30	42x42x42	6	96
Al-steel CMFs	4.0mm	0.38	0.43	0.53	167x167x167	46	248
	5.2mm	0.52	0.60	0.73	14x14x14	4	57

Figure 6–3 shows the neutron transmission prediction for close-cell CMFs with sphere arrangements of SC, BCC, and FCC using the Monte Carlo code (MCNP5) in comparison to the experimental results. It is interesting to find that shielding behaviors exhibit strong dependency on the model assumptions.

In steel-steel CMFs, MCNP5 simulations predict that the SC structure is the most efficient sphere arrangement. This is attributed to the fact that SC structure has lowest packing density, which is a reflection of lowest percentage of air in the structure, and thus results in a higher shielding efficiency. It can be clearly seen from in Figure 6–3 that experimental values fall in between the SC and BCC theoretical curves, which is a good agreement with the model prediction since the actual packing density of spheres in CMFs is falling between the packing density of spheres in SC and BCC. In Al-steel CMFs, the experimental curve still lies in between SC and BCC curves, and are in accordance with our prediction. However, in this case the FCC

structure possessed the highest attenuation efficiency, as shown in Figure 6–4. This can be attributed to the higher sphere packing density in FCC structure and resulted sphere-matrix interfacial area, which is causing the formation of greater amount of intermetallic precipitation along the sphere wall and within the matrix. This study suggests that the presence of intermetallics can have a minor effect on shielding behavior of Al-Steel CMFs.
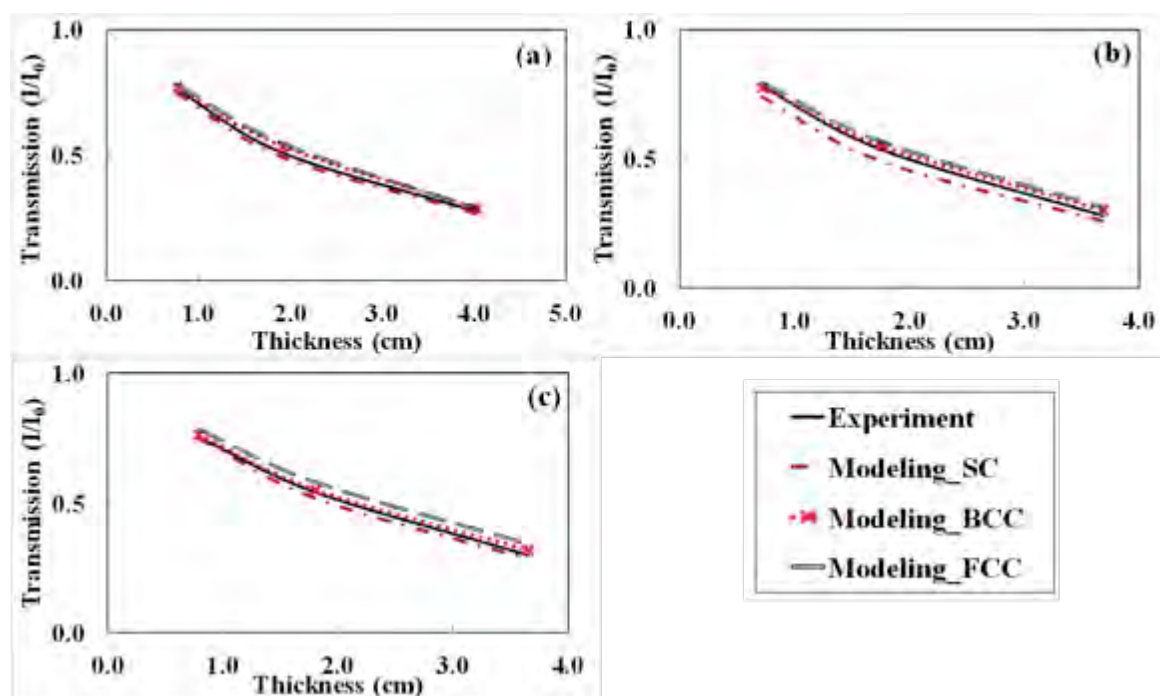

Figure 6–3: Comparison of experimental and theoretical neutron transmission curves for (a) 2.0mm, (b) 4.0mm, and (c) 5.2mm steel-steel CMFs
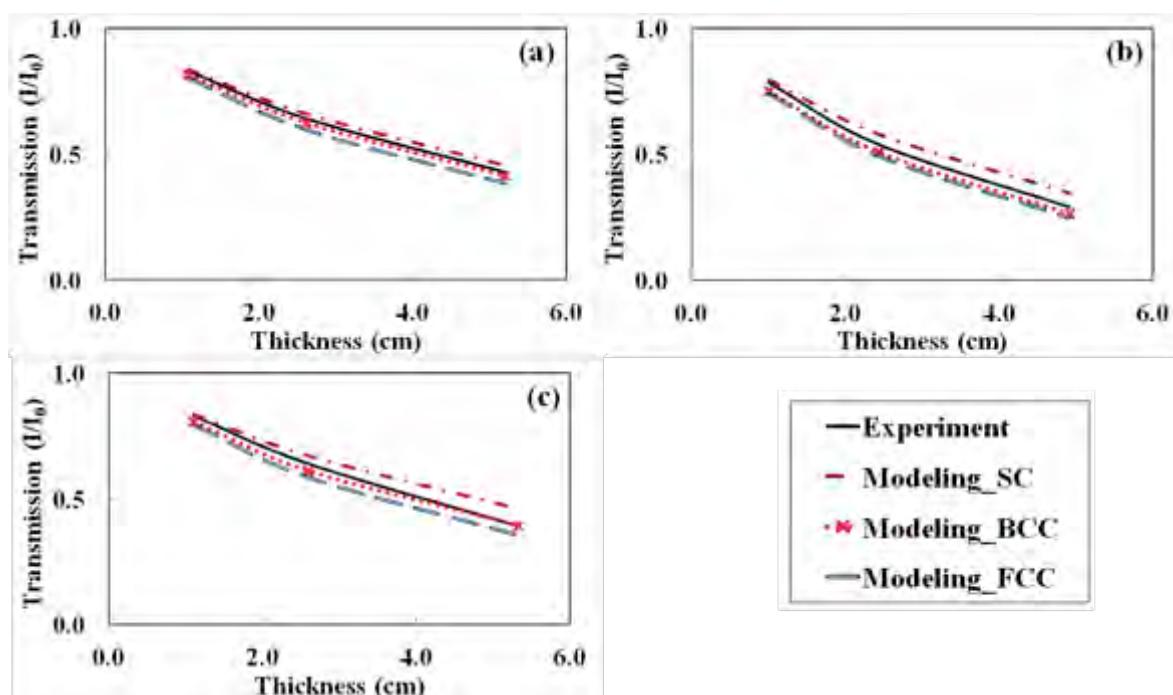
Figure 6–4: Comparison of experimental and theoretical neutron transmission curves for (a) 2.0mm, (b) 4.0mm, and (c) 5.2mm Al-steel CMFs

6.3.2 Modeling of open-cell Al foam with fillers

Open-cell Al foams investigated in this study is made of Al 6101-T6 alloys with 5 pores per inch (5PPI) and 97% porosity (ε_o). Figure 6–5 shows the digital image of an open-cell Al foam. Due to the geometrical complexity and the random orientation of the solid phase of the porous medium, the real geometry of foams is not easy to characterize unless employing geometric idealization by using periodic unit cell. When the structure is periodic, the overall foam is represented by repeating that of a single unit cell, for which two schematic representations have been proposed in this study. In the first approach (Figure 6–6a): three equivalent cylindrical ligaments are intersecting in three mutually perpendicular directions creating the periodic foam geometry. In the second approach (Figure 6–6b): unit cell consists of four cylindrical ligaments in each of the body diagonal direction interconnected at the center of the cell.
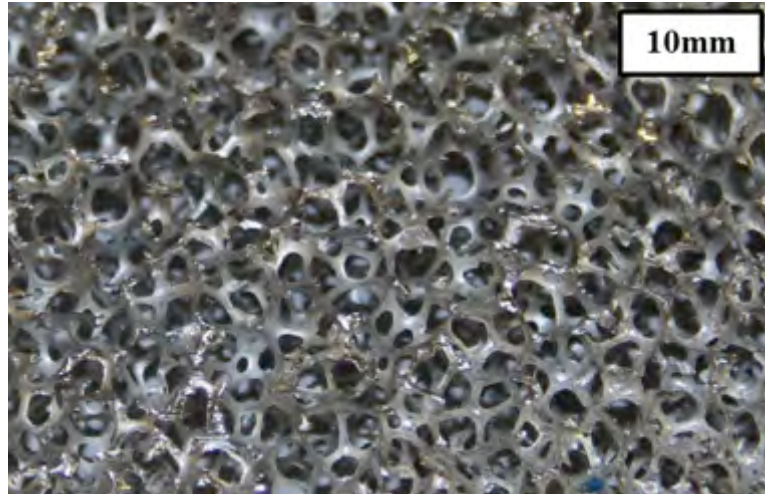
Figure 6–5: Digital image of open-cell Al foam supplied by ERG Aerospace Corporation with 5PPI
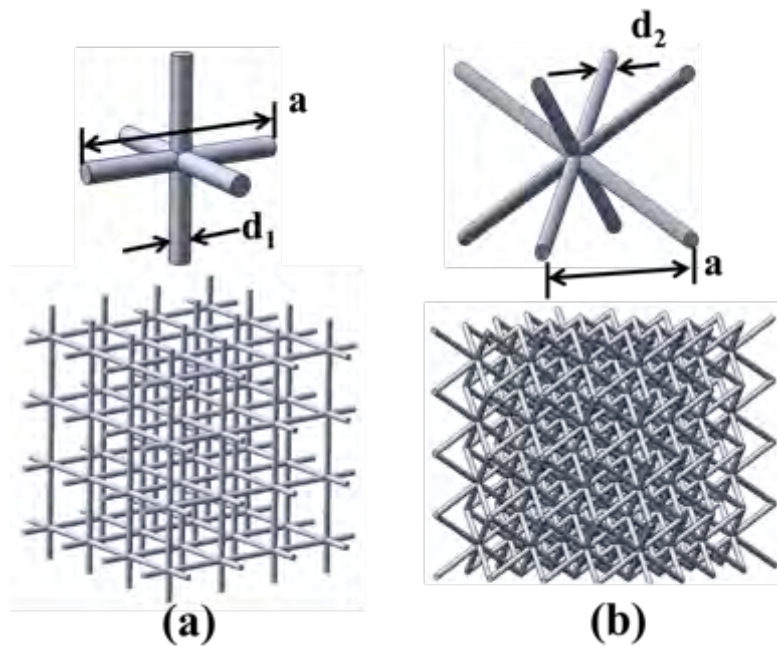

Figure 6–6: Representations of open-cell Al foam (a) Model-1 (b) Model-2

Lattice parameter (a_o) of the unit cell was measured to be 0.473cm, which match the calculated value for 5 PPI foam with an error of ±6.8% as well as the measured values that reported from literature within an error of ±7.5%. Diameter of cylindrical ligaments in Model-1

(d_1=0.0534cm) and Model-2 (d_2=0.0351cm) is thus a function of foam porosity, filler density and lattice parameter, which were calculated through equation (23) and (24), respectively:

$$d_1 = \sqrt{\frac{4(1-\varepsilon_o)a_o^2}{3\pi}}$$

(23)

$$d_2 = \sqrt{\frac{(1-\varepsilon_o)a_o^2}{\sqrt{3}\pi}}$$

(24)

Figure 6–7 shows the comparison of simulated neutron transmission curves using the Monte Carlo code (MCNP5) with experimental data for open cell aluminum foam infiltrated with (a) wax, (b) PE, (c) water and (d) borated water. The figure clearly shows a reasonable agreement between the experimental and the theoretical results. The relative errors between the experimental and model predictions are calculated to be in the range of 11.9% to 14.2% for Model-1 and 10.8% to 14.0% for Model-2. A discrepancy is typically found between analytical models and experimental measurements, which is attributed to the fact that open-cell Al foam is naturally non-periodic, non-uniform and anisotropic, which may lead to deviation of the model presented in this analysis from experimental data. Model-2 provides a slightly better result than that of Model-1, thus, more complexities are necessitated to obtain an improved prediction.
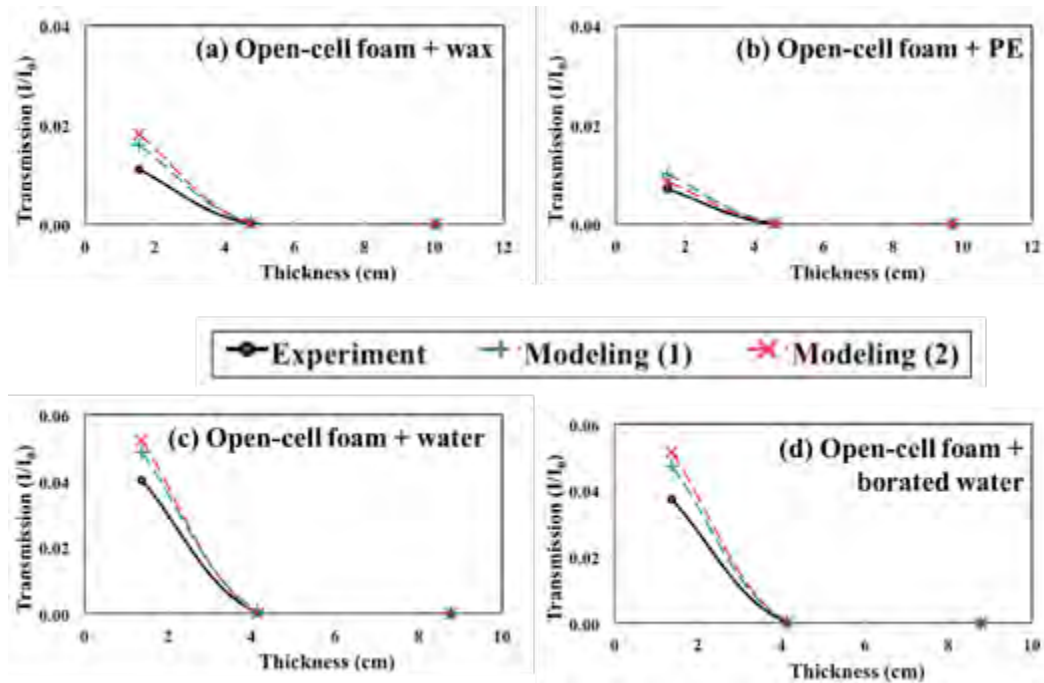

Figure 6–7: Comparison of experimental and theoretical transmission curves for open-cell Al foam with (a) wax, (b) PE, (c) water, and (d) borated water

CHAPTER 7   SUMMARY AND CONCLUSIONS

Close-cell composite metal foams (CMFs) with various sphere sizes, as well as open-cell Al foam with fillers were successfully designed, manufactured, and investigated for nuclear applications in terms of radiation shielding attenuation, thermal and mechanical analyses.

Radiation shielding properties of close-cell CMFs and open-cell Al foam with fillers were studied experimentally and theoretically by means of X-ray, gamma ray and neutrons. In X-ray attenuation study, Al-S CMFs and S-S CMFs were observed to be respectively 145% and 275% more effective than that of Aluminum A356. As compared with pure lead, close-cell CMFs show adequate shielding with additional advantages of environmental friendly, heat rejection and energy absorption capabilities. While in gamma ray studies, it is observed that close-cell CMFs exhibit a better shielding capability compared to open-cell Al foam with fillers. The mass attenuation coefficients of S-S CMFs and Al-S CMFs were measured respectively 400% and 300% higher than that of Aluminum A356 at energies below 0.662 MeV. While in thermal neutron transmission measurements, the results obtained revealed that close-cell CMFs offer better attenuation capabilities compared to aluminum A356, open-cell Al foam with fillers exhibit higher neutron attenuation effectiveness than close-cell CMFs as a results of higher hydrogen content in the filler materials. In order to further enhance the radiation shielding capability of S-S CMFs, high-Z T15 high-speed steel powder containing tungsten (12.5 wt%) and vanadium (5.0 wt%) was introduced into S-S CMFs matrix. The resulting HZ S-S CMFs showed improved shielding efficiency for all three types of radiation, X-ray, gamma ray and neutrons while maintaining its low density and high-energy absorption capabilities. Successful models that link the observed material properties and microstructure have been developed to predict the shielding efficiency of close-cell CMFs and open-cell Al foam with filler. A complete agreement was observed between experimental and the developed theoretical model results.

In thermal and mechanical measurements, CMFs have shown large densification strain that results in high-energy absorption capability, and low thermal conductivity and low coefficient of thermal expansion leading to better dimensional stability. This study indicates the potential of utilizing the lightweight composite metal foams as shielding material replacing current heavy materials used for attenuation of gamma rays, X-rays and thermal neutrons with additional advantages such as high-energy absorption and excellent heat rejection capabilities.

Flame tests also confirmed the higher thermal stability of CMFs compared to steel plates with similar thicknesses.

The CMFs developed and discussed in this work offer extremely good thermal insulation, superior thermal stability, and excellent flame retardant performances as compared to commercially available materials such as stainless steel. Thermal conductivity and coefficient of thermal expansion of CMF is relatively independent of sphere size. It should be noted that the variation of thermal conductivity of S-S CMFs is relatively small under the measured temperature range comparing with solid stainless steel. The desirable characteristics of CMFs, along with other suitable properties such as lightweight, radiation shielding efficiency and energy absorption capability make CMF attractive materials for many structural applications such as nuclear spent fuel casks. This study opens up room for future modifications of the components of CMF materials such as the matrix or sphere wall compositions to further improve their shielding performance, while maintaining their excellent mechanical and thermal properties and offer a novel extra-ordinary material for next generation of nuclear structures and spent fuel casks.

CHAPTER 8   REFERENCES

[1] Khayatt, A.M., "Radiation shielding of concretes containing different lime/silica ratios", Annals of Nuclear Energy, Volume 37, 2010, pp 991-995.

[2] Rabiei, A., Vendra, L.J., "A comparison of composite metal foam's properties and other comparable metal foams", Materials Letters, Volume 63, 2009, pp 533-536.

[3] Rabiei, A., Garcia-Avila, M., "Effect of various parameters on properties of composite steel foams under variety of loading rates", Materials Science and Engineering A, Volume 564, 2013, pp 539-547.

[4] Xu, S., Bourham, M., Rabiei, A., "A novel ultra-light structure for radiation shielding", Materials and Design, Volume 31, 2010, pp 2140-2146.

[5] Chung, D.D.L., "Materials for electromagnetic interference shielding", Journal of Materials Engineering and Performance, Volume 9(3), June 2000, pp 350-354.

[6] Neville, B., Rabiei, A., "Composite metal foams processed through powder metallurgy", Materials & Design, Volume 29, Issue 2, 2008, pp 388-396.

[7] Rabiei, A., Vendra, L.J., "A comparison of composite metal foam's properties and other comparable metal foams", Materials Letters, Volume 63, 2009, pp 533-536.

[8] Chen, S., Bourham, M., Rabiei, A., 2015. Neutrons attenuation on composite metal foams and hybrid open-cell Al foam. Radiat. Phys. Chem. 109, 27–39.

[9] Vendra, L.J., Rabiei, A., "A study on Al-Steel composite metal foam processed by casting", Materials Science and Engineering A, Volume 465, 2007, pp 59-67.

[10] Rabiei, A., Vendra, L., Reese, N., Young, N., Neville, B.P., "Processing and characterization of a new composite metal foam", Materials Transactions, Japan Institute of Metals, Volume 47, 2006, pp 2148-2153.

[11] Rabiei, A., O'Neill, A.T., "A study on processing of a composite metal foam via casting", Materials Science and Engineering A, Volume 404, 2005, pp 159-164.

[12] Chen, S., Bourham, M., Rabiei, A., 2014b. Applications of Open-cell and Closed-cell Metal Foams for Radiation Shielding. Procedia Mater. Sci., 8th International Conference on Porous Metals and Metallic Foams 4, 293–298.

[13] DuJulio, D., Hawari, A., "Examination of reactor grade graphite using neutron powder diffraction", Journal of Nuclear Materials, Volume 392, 2009, pp 225–229.

[14] Shunmugasamy, V.C., Pinisetty, D., Gupta, N., 2012. Thermal expansion behavior of hollow glass particle/vinyl ester composites. J. Mater. Sci. 47, 5596–5604. doi:10.1007/s10853-012-6452-9

[15] Walton, D.G., Blackburn, S.M., 2012. Transportation for the Nuclear Industry. Springer Science & Business Media.

[16] Lowenthal, G.C., Airey, P.L., Practical Applications of Radioactivity and Nuclear Radiations, first ed. United Kingdom: Cambridge University Press; 2001. Chapter 3.

[17] Jevremovic, T., Nuclear Principles in Engineering, second ed. New York: London Springer; 2009. Chapter 6.

[18] Chen, S., Bourham, M., Rabiei, A., "A novel light-weight material for shielding gamma ray", Radiation Physics and Chemistry, Volume 96, March 2014, pp 27-37.

[19] http://rsbweb.nih.gov/ij/index.html

[22] Hütt, M.-T., L'vov, A.I., Milstein, A.I., Schumacher, M., 2000. Compton scattering by nuclei. Phys. Rep. 323, 457–594. doi:10.1016/S0370-1573(99)00041-1

[23] Knoll, G.F., 2000. Radiation Detection and Measurement, third ed. John Wiley and Sons, New Jersey. (Chapter 2), third edition. ed. John Wiley and Sons, New Jersey.

[24] Bloom, E.E., 1998. The challenge of developing structural materials for fusion power systems. J. Nucl. Mater. 258–263, Part 1, 7–17. doi:10.1016/S0022-3115(98)00352-3

[25] Bakhtiyarov, S.I., Overfelt, R.A., Teodorescu, S.G., 2001. Electrical and thermal conductivity of A319 and A356 aluminum alloys. J. Mater. Sci. 36, 4643–4648. doi:10.1023/A:1017946130966

[26] Tien Chih Lin, N.G., 2009. Thermoanalytical characterization of epoxy matrix-glass microballoon syntactic foams. J. Mater. Sci. 44, 1520–1527. doi:10.1007/s10853-008-3074-3

[27] Totten, G.E., MacKenzie, D.S., 2003. Handbook of Aluminum: Vol. 1: Physical Metallurgy and Processes. CRC Press.

[28] Brailsford, A.D., Major, K.G., 1964. The thermal conductivity of aggregates of several phases, including porous materials. Br. J. Appl. Phys. 15, 313. doi:10.1088/0508-3443/15/3/311

[29] Turner, P.S., 1946. Thermal-expansion stresses in reinforced plastics. J. Res. Natl. Bur. Stand. 37.

[30] Nji, J., Li, G., 2008. A CaO enhanced rubberized syntactic foam. Compos. Part Appl. Sci. Manuf. 39, 1404–1411. doi:10.1016/j.compositesa.2008.05.001

[31] Kulesa, A.T., Robinson, M.J., 2015. Analytical study of structural thermal insulating syntactic foams. Compos. Struct. 119, 551–558. doi:10.1016/j.compstruct.2014.09.025